crystals

Review

Ferroelectric/Piezoelectric Materials in Energy Harvesting: Physical Properties and Current Status of Applications

Maria-Argyro Karageorgou, Kosmas Tsakmakidis and Dimosthenis Stamopoulos *

Department of Physics, School of Science, National and Kapodistrian University of Athens, Zografou Panepistimioupolis, 15784 Athens, Greece; kmargo@phys.uoa.gr (M.-A.K.); ktsakmakidis@phys.uoa.gr (K.T.)
* Correspondence: densta@phys.uoa.gr

Abstract: The inevitable feedback between the environmental and energy crisis within the next decades can probably trigger and/or promote a global imbalance in both financial and public health terms. To handle this difficult situation, in the last decades, many different classes of materials have been recruited to assist in the management, production, and storage of so-called clean energy. Probably, ferromagnets, superconductors and ferroelectric/piezoelectric materials stand at the frontline of applications that relate to clean energy. For instance, ferromagnets are usually employed in wind turbines, superconductors are commonly used in storage facilities and ferroelectric/piezoelectric materials are employed for the harvesting of stray energy from the ambient environment. In this work, we focus on the wide family of ferroelectric/piezoelectric materials, reviewing their physical properties in close connection to their application in the field of clean energy. Among other compounds, we focus on the archetypal compound $Pb(Zr,Ti)O_3$ (or PZT), which is well studied and thus preferred for its reliable performance in applications. Also, we pay special attention to the advanced ferroelectric relaxor compound $(1-x)Pb(Mg_{1/3}Nb_{2/3})O_3-xPbTiO_3$ (or PMN-xPT) due to its superior performance. The inhomogeneous composition that many kinds of such materials exhibit at the so-called morphotropic phase boundary is reviewed in connection to possible advantages that it may bring when applications are considered.

Keywords: energy harvesting; piezoelectricity; ferroelectrics; PZT; PMN-xPT; morphotropic phase boundary; clean energy

check for updates

Citation: Karageorgou, M.-A.; Tsakmakidis, K.; Stamopoulos, D. Ferroelectric/Piezoelectric Materials in Energy Harvesting: Physical Properties and Current Status of Applications. *Crystals* **2024**, *14*, 806. https://doi.org/10.3390/cryst14090806

Academic Editor: Peng Shi

Received: 20 August 2024
Revised: 6 September 2024
Accepted: 10 September 2024
Published: 12 September 2024

1. Introduction

Clean energy harvesting has received significant interest, not only in the academic field but also in the industrial field, due to the fact that it gives the potential for the development of autonomous and sustainable electronic devices. Such a mechanism decreases the danger of the greenhouse effect and global warming and protects the environment from pollution [1]. Conventionally, electronic devices were powered by batteries. Energy harvesting devices scavenge stray energy found in the ambient environment in the form of mechanical vibrations, thermal fluctuations, wind, light, fluid flows, etc. in order to generate electrical power. The capability of providing sustainable power to electrical equipment, including wireless networks, mobile electronics, sensors, implantable medical devices, etc., through energy harvesting is appealing due to the expense of batteries, the time and cost for their replacement, and their recharging and maintenance, as well as their bulky size, which burdens the miniaturization of the devices.

Due to its abundance in nature, mechanical energy is the most prevalent form of energy; hence, it is widely exploited. Piezoelectric materials, which were discovered by Pierre and Jacques Curie in 1880, constitute a promising class of materials for harvesting mechanical energy, as the piezoelectric effect (PE) is dependent on the intrinsic property of materials' polarization. In particular, piezoelectric materials are polarized upon the influence of tensile or compressive stress, in this way generating electrical voltage. For this reason, compared to conventional mechanical energy harvesters, energy harvesting based on piezoelectric materials provides devices in current or future applications with several advantages, including endurance, pliability, increased sensitivity to minor strains, higher density power and voltage outputs, and adaptability for integration into complicated systems [2–4].

A system for energy harvesting consists of the source from which the energy is harvested to produce electrical energy, the harvesting unit for converting the energy into electrical power and the load, where the electrical output energy is consumed or stored [5]. The ratio of the consumed power on the load and the overall mechanical power input provides the efficiency of the energy harvester. The ratio of the consumed power on the load to the converted electrical power corresponds to the electrical efficiency, while the mechanical efficiency is calculated by dividing the converted electrical power by the overall mechanical power input [6]. The percentage of the efficiency of energy conversion (E) can be found by the ratio of the electrical (E_e) and the mechanical (E_m) energy, according to the equation below:

$$\%E = \frac{E_e}{E_m} \times 100 \tag{1}$$

where E_e and E_m are defined as:

$$E_e = P\Delta t = \frac{V^2}{R}\Delta t \tag{2}$$

$$E_m = \int_0^{\Delta t} \mathbf{F}(\mathbf{t})\mathbf{d}(t)dt \tag{3}$$

where $\mathbf{F}$(t) corresponds to the applied force, $\mathbf{d}$(t) is the displacement due to the applied force, P and V are the output power and voltage, respectively, and R is the resistive load [7].

The scope of this review is to provide comprehensive information concerning the energy harvesting applications associated with piezoelectric materials and their subclass—ferroelectric materials [8–25]. Thus, the review paper is structured as follows: initially, a description of the basic concept of piezoelectricity is provided (Section 2), followed by a reference to piezoelectric and ferroelectric materials, focusing on lead-zirconate-titanate, $Pb(Zr_xTi_{1-x})O_3$ and $(1-x)Pb(Mg_{1/3}Nb_{2/3})O_{3-x}PbTiO_3$ (Section 3). After the basic properties of piezoelectric and ferroelectric materials are known, energy harvesting applications found in the literature are mentioned (Section 4). In the final section of this paper (Section 5), conclusions are provided.

2. Piezoelectricity

Piezoelectricity (coming from the Greek word that means squeeze or press) defines the property of certain materials to transform mechanical stress into electrical energy. When mechanical stress (tensile or compressive) is applied to a piezoelectric material, it generates spatially separated opposite electric charges across its surfaces. When the applied mechanical stress is removed, the material returns to its uncharged state (or its mechanical deformation is restored), leading to the conversion of mechanical energy to electrical energy, a phenomenon known as the direct piezoelectric effect (PE). Conversely, when an electric field is applied to a piezoelectric material in the direction of polarization, it undergoes macroscopically mechanical strain, known as converse or PE [8]. A simplified illustration of both effects is depicted in Figure 1a for a plate-shaped sample. As shown, referring to the direct PE, the application of an external mechanical stress along the z axis, $T_{ex,z}$, induces dielectric displacement, D_z. Referring to the converse PE, the application of an external electric field along the z axis, $E_{ex,z}$, induces mechanical strain along the x and y axes, namely S_x and S_y, respectively. The equations for the direct and converse PE effect in tensor form are expressed as:

$$D_i = d_{ij}T_j \tag{4}$$

$$S_j = d_{ij}E_i \tag{5}$$

with i = 1–3 and j = 1–6. The piezoelectric coefficient, d_{ij}, corresponds to the charge generated per unit of applied stress, T, or the strain induced per unit of applied electric field, E. It is expressed by the equations:

$$d_{ij} = \left(\frac{\partial D_i}{\partial T_j}\right)^E \tag{6}$$

$$d_{ij} = \left(\frac{\partial S_j}{\partial E_i}\right)^T \tag{7}$$

where the upper index denotes constant electric and stress field, respectively [9,10]. Equations (4) and (5) correspond to PE materials, which, as we discuss below, constitute a subclass of dielectric materials. Owing to the electrostrictive effect, the presence of an electric field induces strain, even for the general case of dielectrics, and thus, the strain is a quadratic function of the applied field. In realistic strain–electric field curves of piezoelectrics, both piezoelectric and electrostrictive effects contribute.

The polarization–electric field hysteresis loop is a defining and important characteristic of ferroelectric materials (Figure 1b). At zero electric field, the unpolarized material shows a multi-domain structure due to the need for energy minimization. The polarization in each domain is randomly oriented, leading to a zero net polarization in the material. According to Figure 1b, when the externally applied electric field is increased from zero, the polarization progressively increases in a non-linear way, tracing the indicative curve A-B-C. Firstly, a slow increase in polarization is observed, and subsequently, it becomes more abrupt until the polarization reaches saturation (at points C, E). At the point at which polarization saturates, the orientation of almost all of the domains in the material is parallel to the direction of the applied electric field; hence, a homogeneous polarization throughout its entire volume appears. By decreasing the electric field (tracing the line C-D-F), some of the domains will back-switch, and when the electric field becomes zero, the polarization will obtain a non-zero value called remanent polarization, P_r (point D). This is because, in this state, some of the domains in the material are still oriented towards their former direction. When the field is reversed in the opposite direction, the polarization progressively decreases. The electric coercive field, E_c (point F), corresponds to a field where polarization becomes value. A subsequent increase in the electric field in the opposite direction (tracing the line F-G) provokes the reversal and alignment of the ferroelectric domains towards the new direction of the electric field; hence, the polarization reaches negative saturation (at point G). The hysteresis is formed when the loop closes upon the field cycling back [22,23].

The piezoelectric effect typically arises in materials with crystal structure, which show the absence of a center of symmetry in their unit cell (as in ZnO, $BaTiO_3$, and PZT), giving rise to the existence of spontaneous electric polarization (which means that they maintain the polarization even after the removal of the external electric field) [11]. Consequently, the application of a mechanical stress in a material with a non-centrosymmetric crystal structure provokes the displacement of the centers of positive and negative charges, hence generating electric polarization in it. Similarly, the application of an electric field provokes the mechanical deformation of such non-centrosymmetric unit cells.

Piezoelectric materials constitute a general family of materials that also include two subclasses: pyroelectrics and ferroelectrics. The present review focuses on the application of piezoelectric and ferroelectric materials in energy harvesting. Thus, information concerning pyroelectric materials and their subsequent application in pyroelectric energy harvesting are not discussed here. On the other hand, the subset of piezoelectric materials in which the application of an electric field reorients the spontaneous polarization vector is known as ferroelectric materials [12].

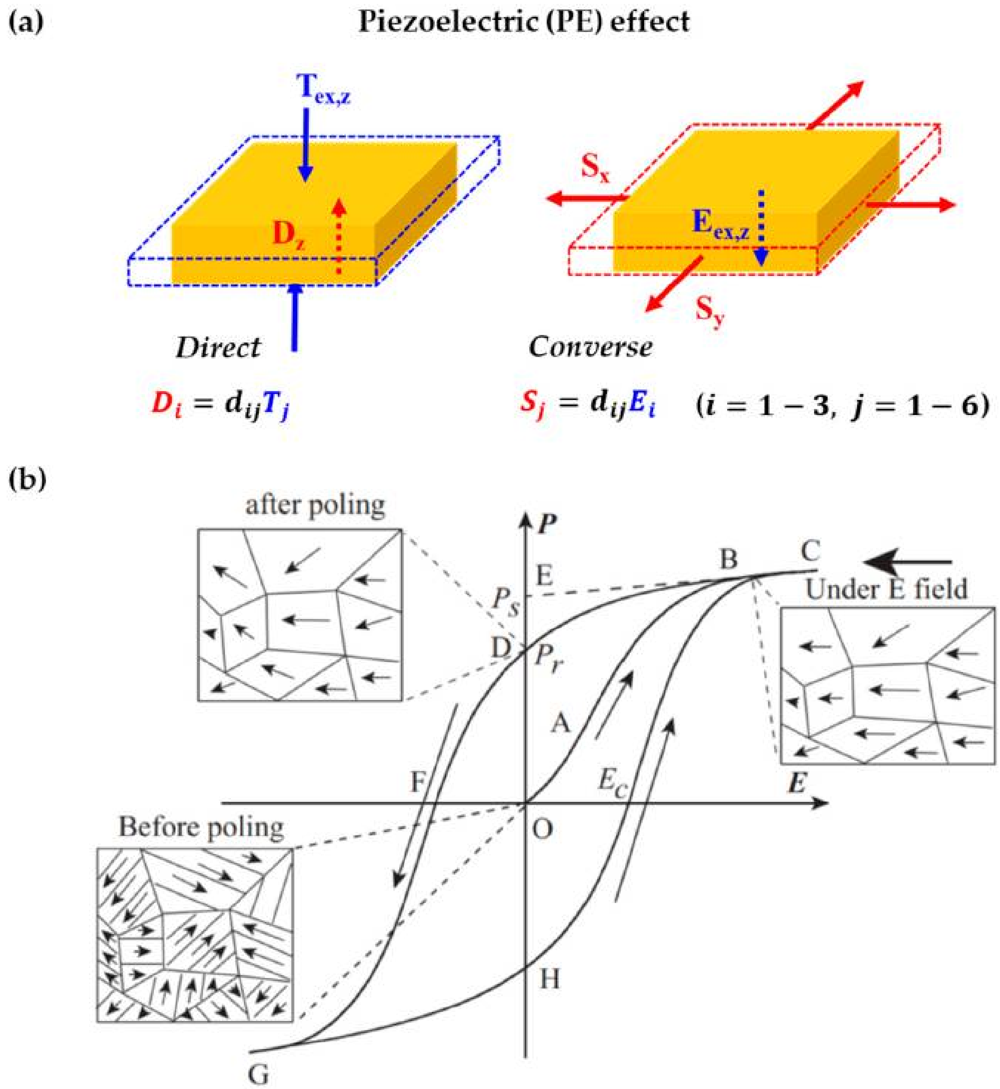

Figure 1. (**a**) Direct and converse PE effect for a plate-shaped sample. An externally applied mechanical stress along z axis, $T_{ex,z}$, induces electric displacement, D_z. An externally applied electric field along z axis, $E_{ex,z}$, induces mechanical strain along x and y axes, namely S_x and S_y, respectively. Their constitutive relations are also depicted in tensor form, where the externally applied tensors are illustrated in blue, namely the mechanical stress, T_j, and the electric field, E_i, while the induced tensors are shown in red, namely the dielectric displacement, D_i, and the strain, S_j; (**b**) polarization (P)–electric field (E) hysteresis loop of ferroelectrics. P_s and P_r correspond to spontaneous and remnant polarization, respectively, and E_c corresponds to the coercive field. The corresponding reversal of polarization in the domains after the application of E is also depicted (copyright (2014) Wiley; used with permission from [23]).

Referring to ferroelectricity, the absence of symmetry of the crystal structure below a phase transition temperature, namely the Curie temperature, leads to the development of spontaneous polarization in these materials. Above the Curie temperature, the symmetry of the crystal structure increases while the spontaneous polarization disappears, and the material becomes paraelectric. Thus, the significant interest in ferroelectric materials arises from their intrinsic property of spontaneous polarization and the ability to reorient and even reverse their direction upon the application of an electric field. The degree of polarization can be affected by external stimuli, such as vibrations, stress, and light. These properties render ferroelectrics powerful tools for the development of energy harvesting devices, ultimately providing the opportunity to produce electrical energy from various stimuli.

The application of mechanical stress to a ferroelectric material alters the spontaneous polarization, ultimately leading to a change in the distribution of bound (volume and surface) charges, with the surface ones being the dominant contributor. Accordingly, the surface charges mainly accumulate at the opposite surfaces of the ferroelectric material. The electric field created by this change in polarization can drive these charges to effectively become free and move through an external circuit. Ultimately, this generates a current that is crucial for piezoelectric harvesters' operation [13].

The performance of a piezoelectric harvesting system is proportional to the square of the piezoelectric coefficient, d^2, and inversely proportional to the dielectric permittivity, ε [14]. The piezoelectric materials exhibit two common configurations for energy harvesting operation (Figure 2), the 33-mode (Figure 2a) and the 31-mode (Figure 2b), depending on the direction of the applied stress relative to the material's polarization direction. The polar axis is defined as the "3" direction, while all directions perpendicular to the polar axis are defined as "1" directions [15]. When the direction of the applied stress is parallel to the polar axis, the coupling mode is 33-mode, while when it is perpendicular to the polar axis, the coupling mode is 31-mode. In both coupling modes of operation (31 and 33), the electrodes are mounted at right angles to the polar axis; namely, the direction of the electric field and the polarization are aligned.

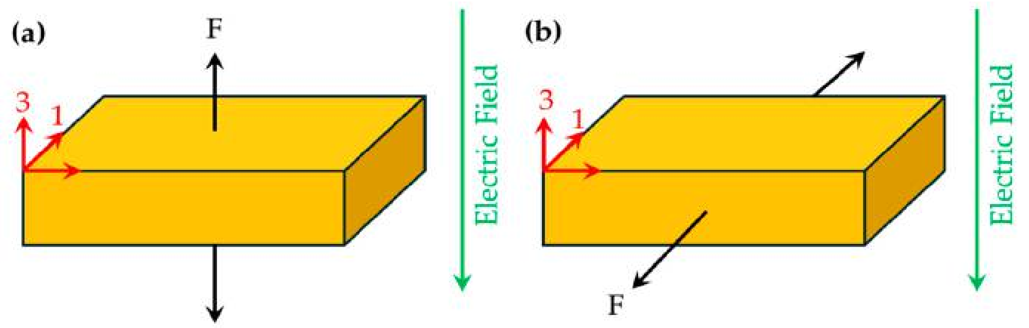

Figure 2. Configurations for energy harvesting operation: (**a**) 33-mode and (**b**) 31-mode.

The geometrical configurations of piezoelectric transducers play a significant role in their power efficiency. The most common ones are the unimorph and bimorph cantilever beam configurations since they undergo increased mechanical strain upon vibration, leading to high power efficiency [16]. An example of these configurations is depicted in Figure 3. As shown, the unimorph configuration of the piezoelectric cantilever (Figure 3a) uses only one piezoelectric layer that is bonded with a non-piezoelectric material (such as metal, etc.), also in the form of a layer. Its one end is fixed in order to exploit its bending mode. On the other hand, the bimorph configuration of the piezoelectric cantilever (Figure 3b) uses two piezoelectric layers bonded at the opposite sides of an interlayer of a non-piezoelectric material [17]. In piezoelectric energy harvesting, the bimorph configuration is more common since it doubles the electrical energy output while barely modifying the volume of the energy harvesting device. In a study, low-level vibrations were harvested by a 1.75 cm PZT piezoelectric bimorph cantilever. In order to reduce the resonance frequency, a proof mass was placed at the cantilever's tip, matching the harvester's natural frequency of 100 Hz. As a result, they were able to obtain 60 W of power [18].

In a piezoelectric cantilever, the piezoelectric layers are polarized perpendicular to their planar direction, operating in the 31-mode. This mode is determined by the d_{31} piezoelectric charge constant, which is generally smaller than the respective one of 33-mode because the stress is not applied along the piezoelectric material's polar axis. To employ the 33-mode, which provides higher electrical energy output, interdigitated electrodes are placed alternately on the piezoelectric sheet's surface (Figure 3c), leading the electric field laterally during polarization. This lateral polarization aligns with the stress direction during bending, allowing the primary d_{33} charge constant to be used. Moreover, a proof mass is attached at the free end of the cantilever in order to lower its resonance frequency

(Figure 3d). Lowering the resonant frequency is beneficial, particularly for applications of harvesting energy from low-frequency vibrations [17].

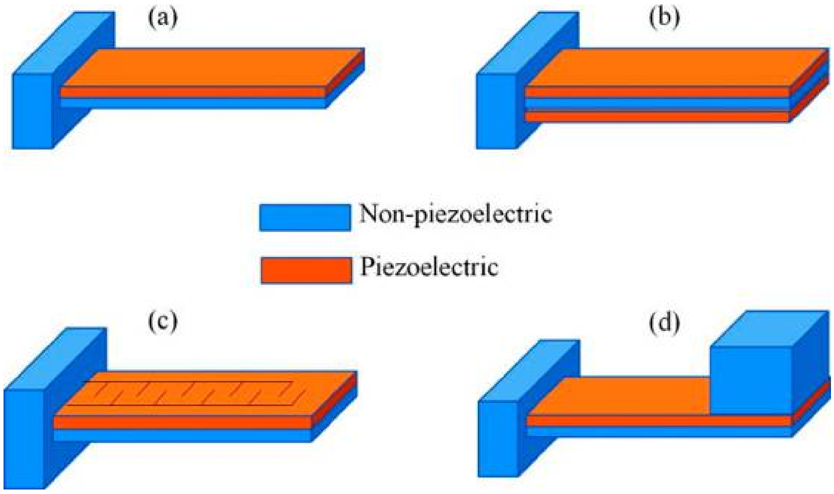

Figure 3. (**a**) Unimorph and (**b**) bimorph cantilever beam configurations; (**c**) cantilever with interdigitated electrodes; (**d**) cantilever with proof mass at its free end (reprinted with permission from [17], copyright (2014), with permission from AIP Publishing).

3. Piezoelectric and Ferroelectric Materials

Ferroelectrics constitute a well-studied subclass of piezoelectric materials due to their responses to electric, mechanical, thermal, and optical fields, leading to a wide range of ferroelectric-based device applications [19]. They are oxides and show a perovskite crystal structure, namely ABO_3, where A cations (either monovalent or bivalent) are placed at the edges of the unit cell, B cations (either tetravalent or pentavalent) occupy the center, and O^{2-} are oxygen ions found at the face centers (Figure 4a). Perovskite is the dominant piezoceramic crystal structure among others (such as ilmenite, bismuth-layer, etc.) due to its exceptional efficiency; thus, it constitutes the center of interest for many researchers. At temperatures higher than Curie temperature, due to this highly centrosymmetric cubic (a = b = c) structure, ferroelectrics exhibit paraelectric properties. On the contrary, at temperatures smaller than Curie temperature, ferroelectrics undergo a structural phase transition (from cubic, a = b = c, to tetragonal, a = b $\neq$ c) that is related to the existence of spontaneous polarization. Specifically, the displacement of B cation in the unit cell off-center relative to the oxygen O^{-2} anions (Figure 4b) is correlated with the existence of spontaneous polarization, which comes from the electric dipole moment created by this displacement. The direction of spontaneous polarization can be switched to the preferred polarization axis, shown by the dashed arrow in Figure 4b. Furthermore, spontaneous polarization is associated with the existence of piezoelectric properties in these materials. The transition occurs in order to reduce the electrostatic energy, which is produced by the surface charge at T_{curie} (depolarizing field), and the corresponding elastic energy, linked with the mechanical constraints to which the ferroelectrics undergo [20,21].

As already mentioned above in the discussion of Figure 1b, the polarization–electric field hysteresis loop is an important characteristic of ferroelectric materials [22,23]. While Figure 1b refers to a schematic illustration of a realistic case that exhibits a smooth modulation of polarization upon variation of the electric field, in Figure 5a below, we present a schematic illustration for the ideal case of a completely orthogonal hysteresis loop, P-E_{ex} [22,23]. As depicted, the orthogonal loop is symmetric, and the negative and positive coercive fields, -Ec (point C) and Ec (point F), are equal. The same stands for -P_r (point E) and P_r (point B). The positive and negative saturation values of the polarization, P_s, are denoted by the points A and D, respectively, and practically coincide with the remanent polarization, P_r, due to the shape of the loop. Figure 5c shows real experimental data of P in relation to the $E_{ex,z}$ for a PMN-0.30PT single crystal that fairly approximates a completely orthogonal polarization–electric field hysteresis loop (see below) [24,25].

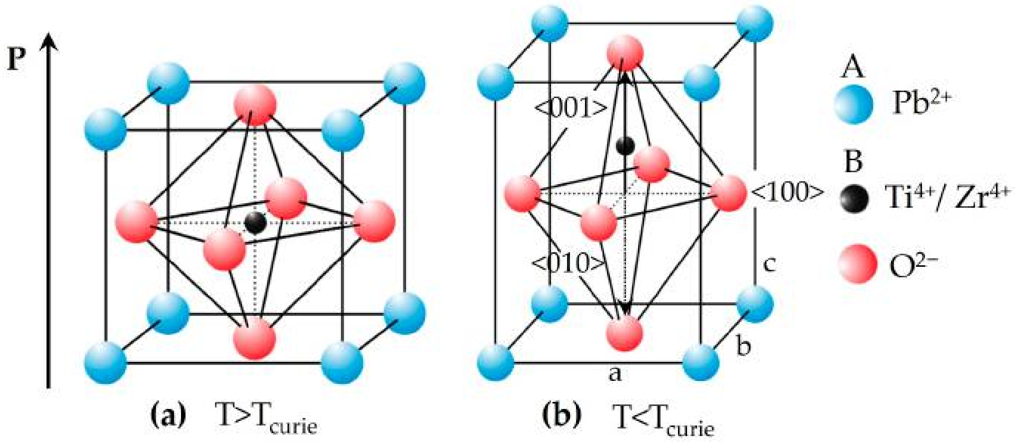

Figure 4. The unit cell of PZT with perovskite-type ABO_3 at (**a**) T > T_{curie} and (**b**) T < $_{Tcurie}$. Pb^{2+} and Ti^{4+}/Zr^{4+} ions occupy A and B sites, respectively, while O^{2-} ions are located at the surface centers. The dashed arrow inside the octahedron of panel (**b**) corresponds to the equivalent direction of polarization (P). The solid arrow indicates the direction of P and the displacement of the central B+ cation.

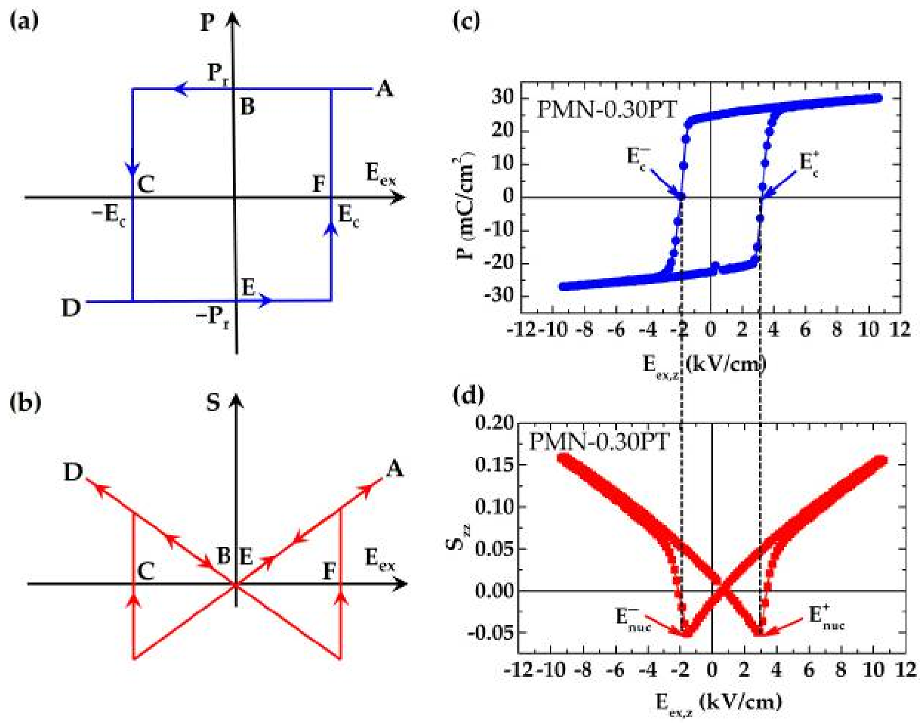

Figure 5. Ideal (**a**) polarization (P)–electric field (E_{ex}) and (**b**) strain (S)–electric field (E_{ex}) hysteresis loops of ferroelectric materials. The characteristic points of the loops are denoted by the capital letters; (**c**) polarization (P)–electric field ($E_{ex,z}$) and (**d**) strain (S_{zz})–electric field ($E_{ex,z}$) hysteresis loops of PMN-0.30PT single crystal upon varying the $E_{ex,z}$ within −10 kV/cm and 10 kV/cm. The coercive and nucleation fields, $\pm E_c$ and $\pm E_{nuc}$, are also indicated by the blue and red arrows, respectively.

Going a step further, another fundamental property is the strain–electric field hysteresis loop, also known as the butterfly loop, owing to its shape that resembles a butterfly [24,25]. This is shown in Figure 5b,d for the ideal schematic case of the perfectly orthogonal and the realistic experimental case of approximately orthogonal, polarization–

electric field hysteresis loops of Figure 5a,c, respectively. In reality, the ferroelectrics' strain–electric field hysteresis demonstrates a non-linear behavior of the materials that is essential for a variety of applications, including actuators and sensors, and shows how the strain evolves in response to small changes in the electric field. This hysteresis loop is formed owing to both the converse piezoelectric effect and the switching and movement of the domain walls [20]. According to Figure 5b, the strain is zero when there is no applied electric field. However, when the ferroelectric material is subjected to an electric field that is applied in the direction of its spontaneous polarization, the dipoles within the material start to align, inducing a small strain. As the electric field increases, the material expands due to the piezoelectric effect until reaching the maximum field (point A). When the electric field is decreased (but it remains in the direction of saturation polarization), the strain decreases, tracing the line A-B and eventually passing through zero when the electric field reaches zero value. As the electric field becomes antiparallel to spontaneous polarization obtaining negative values, the material contracts with respect to the zero point. When the electric field reaches the maximum value, the material's polarization is aligned parallel to the field and the strain again becomes positive. Upon further increase of the electric field in the negative direction, the strain increases in the positive direction (point D). As the electric field is decreased, the strain decreases back to zero [20].

Figure 5c,d indicate real experimental data of P in relation to the $E_{ex,z}$ and the S_{zz} in relation to the $E_{ex,z}$ for a PMN-0.30PT single crystal upon varying the $E_{ex,z}$ within -10 kV/cm and 10 kV/cm. The strain tensor is referred to as S_{zz} in order to highlight the direction of the applied electric field, which is the first subscript, and the direction of the induced strain, which is the second subscript. Referring to the $P(E_{ex,z})$ hysteresis loop, it exhibits a rather tetragonal shape with relatively small E_c (± 2.6 kV/cm). This is because, in a single crystal, such as PMN-0.30PT, the domains undergo a complete switch with respect to the $E_{ex,z}$ compared to polycrystalline materials, whose polarization undergoes a switch up to 83% at maximum [9,10]. Referring to the $S_{zz}(E_{ex,z})$ hysteresis loop, it exhibits two minima, namely $E_{nuc} = \pm 2.5$ kV/cm. As illustrated, these minima appear at electric fields that are slightly smaller than E_c. The term E_{nuc} refers to the nucleation fields, which express the onset of polarization switch, namely where the domains start to move and rotate, resulting in a complete switch of polarization [20,24,26].

Additionally, ferroelectric materials undergo structural phase transition not only at the Curie temperature but also upon decreasing the temperature or by modifying their stoichiometry, resulting in a phase diagram (temperature T (K) versus composition (x)) of ferroelectrics (Figure 6). The morphotropic phase boundary (MPB) constitutes a small region in the phase diagram where two or more structural phases coexist, hence allowing the easier rotation of spontaneous polarization in various directions. The inhomogeneous composition of ferroelectric materials in the MPB results in their enhanced piezoelectric properties (such as increased electromechanical coupling, high dielectric properties and piezoelectric coefficients, etc.) that can offer several benefits for multiple applications of high performance, including energy harvesting [19].

Piezoelectric materials have evolved into four main categories: (i) single crystals, including Rochelle salt, PMN-xPT, lead zirconate niobate–lead titanate (PZN-PT), and quartz crystals; (ii) (piezo)ceramics, including barium titanate ($BaTiO_3$) and PZT; (iii) (piezo)polymers, such as poly(vinylidene fluoride) (PVDF), polylactic acid (PLA), and co-polymers poly(vinylidene fluoride-trifluoroethylene) (P(VDF-TrFE)); and (iv) (nano)composites, including polyvinylidene fluoride-zinc oxide (PVDF-ZnO), cellulose $BaTiO_3$, and polyimides-PZT [27]. The choice of the material employed in an energy harvesting system plays a significant role in its capability and performance. For example, ceramics exhibit high dielectric and piezoelectric coefficients and electromechanical coupling factors, but they are damaged when absorbing high strains. Polymers can withstand high strain, but they have low electromechanical coupling factors. On the other hand, composites possess the advantages of both piezoceramics and piezopolymers, which, however, are utilized in particular applications [4].

The most widely used material for piezoelectric energy harvesting applications is $Pb(Zr_{1-x}Ti_x)O_3$ (shorted as PZT_x), and its subcategories, PZT-5A and PZT-5H, constitute the most popular and implemented ceramic materials. PZT_x has a perovskite crystal structure, shown in Figure 4. In the paraelectric phase (i.e., at $T > T_{curie}$) (Figure 4a), the structure is cubic (a = b = c), and the cations Pb^{2+} and Ti^{4+}/Zr^{4+} occupy the A and B sites, respectively. A remarkable property of this compound is the existence of MPB in its T-x phase diagram. The appearance of MPB results in composition-induced ferroelectric-to-ferroelectric phase transitions. The compositions close to this boundary show significant electromechanical properties [28]. The T-x phase diagram of PZT_x is depicted in Figure 6a. As already mentioned above, at $T > T_{curie}$, its behavior is paraelectric with a cubic crystal structure. The concentration of Ti increases at room temperature, resulting in a structural phase transition. Specifically, this phase transition is performed from the Zr-rich rhombohedral (R) region to the Ti-rich tetragonal (T) region. Both the rhombohedral and the tetragonal structures are ferroelectric. The rhombohedral phase contains the low-temperature one with tilted oxygen octahedra and the high-temperature one with regular non-tilted oxygen octahedra. The transition from the low-temperature to the high-temperature rhombohedral phase corresponds to T_T. At $x \approx 0.48$, the MPB separates the R and T phases. As shown in Figure 6a, there is a narrow area around the composition $x \approx 0.48$, which corresponds to the appearance of an intermediate monoclinic phase (M_A) [29]. The M_A phase constitutes the primary cause of PE property maximization. Furthermore, in the M_A phase, the direction of P_s is intermediate between the R and T phases; thus, it is allowed to rotate continuously between them (shown in the red region of Figure 6(ci)) [30–32]. Consequently, the high PE efficiency at MPB results from the reorientation of P_S with the applied E_{ex} among several available orientations, a characteristic known as the polarization rotation model.

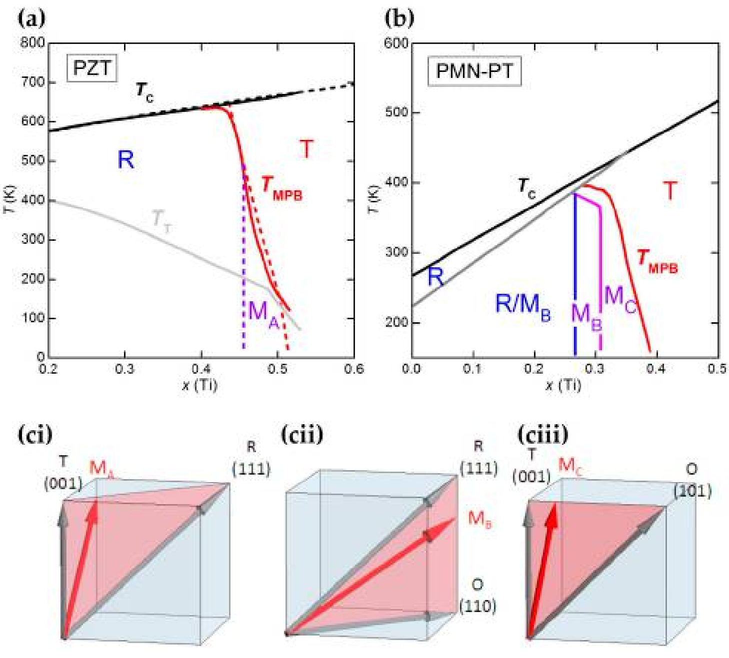

Figure 6. Phase diagrams of (**a**) $Pb(Zr_{1-x}Ti_x)O_3$ (PZT_x) and (**b**) $(1-x)Pb(Mg_{1/3}Nb_{2/3})O_3$–$xPbTiO_3$ (PMN-xPT); (**c**) the red arrows and the corresponding red regions indicate the directions of spontaneous polarization, P_S, in the three types of monoclinic phases: (**ci**) M_A, (**cii**) M_B, and (**ciii**) M_C [32].

PZT displays excellent piezoelectric properties, including high piezoelectric charge (*d*) and voltage (*g*) constants, dielectric constant, electromechanical coupling coefficient, and energy density; hence, it constitutes a promising candidate for high-performance applications [25,33]. Furthermore, a variety of soft and hard PZT-based materials have been constructed by modifying the content of Zr and doping with different elements, such as Mn, Nb, La, Cu, Fe, etc. Modified PZT compositions close to MPB (that is, for $x \approx 0.52$), which exist in between the tetragonal (Ti-rich phase for $x < 0.52$) and rhombohedral phases (Zr-rich phase for $x > 0.53$), cover over 90% of applications, owing to the highest piezoelectric property in this region.

Relaxor ferroelectrics are a subclass of ferroelectric materials. A typical example of this category is a solid solution of $(1-x)Pb(Mg_{1/3}Nb_{2/3})O_3-xPbTiO_3$ (or PMN-xPT) with a perovskite crystal structure (shown in Figure 4). The PMN solid solution, which belongs to relaxor ferroelectrics, with its PT compound, which belongs to conventional ferroelectric materials, forms the phase diagram provided in Figure 6b. As in the case of PZT, at $T > T_{curie}$, PMN-xPT has a cubic crystal structure and shows paraelectric properties. However, at room temperature, it exhibits FE properties and obtains the crystallographic phases (i) R/M_B (M_B monoclinic with pseudorhombohedral features) for $x \leq 0.27$, (ii) M_B for $0.27 \leq x \leq 0.30$, (iii) M_C for $0.31 \leq x \leq 0.40$, and (iv) T for $x > 0.40$. Moreover, it has been reported that at room temperature, the MPB for PMN-xPT can be found in the compositional range from 0.30 to 0.37 [34,35]. The direction of P_s in the M_B and M_c monoclinic phases is illustrated in Figure 6(cii,ciii), respectively. As clearly shown, in the monoclinic phase M_B, the continuous rotation and switching of P_s is performed between the R and orthorhombic (O) phases (Figure 6(cii)), while in the monoclinic phase M_c, it is performed between T and O phases (Figure 6(ciii)) [32]. Additionally, it is worth mentioning that polycrystalline PMN-0.30PT exhibits a high piezoelectric response at $x \approx 0.30$, indicating $d_{33} \approx 700$ pm/V. Similarly, PMN-0.30PT single crystals exhibit an ultra-high piezoelectric response with $d_{33} \approx 2500$ pm/V and $S_{33} \approx 5 \times 10^{-3}$, owing to the polarization rotation in monoclinic phases M_B and M_C, which serve as structural bridges among the R, T, and O crystallographic phases [31,36–38]. The piezoelectric constant of the MPB composition crystal is higher than 2000 pC/N, while its electromechanical coupling coefficient exceeds 0.9, indicating efficient energy conversion between electrical and mechanical forms. Moreover, PMN-xPT provides a piezoelectric coefficient that is 10 times higher than the one for conventional ceramics [39].

Wind is a preferable source for energy harvesting to produce sustainable electric power generation [40]. Pobering et al. developed a wind energy harvesting system that produced electrical power from flowing media without employing any rotating parts [41]. The harvester consisted of two PZT layers with three electrodes on the top, on the bottom, and between these layers. Each cantilever was placed behind a rectangular-shaped bluff body in the streaming direction. The body was used to disturb the flow and to mechanically support the cantilever. The electrical voltage was produced due to mechanical stress changes in the PZT materials, which led to a charge separation on the electrodes. The experimental results of the study showed that the output voltage and the maximum output power were found to be 0.8 V and 0.1 mW, respectively, for 45 ms^{-1} wind speed. Bryant et al. employed a PZT piezoelectric cantilever beam with a wing configuration embedded at its free end in order to harvest wind energy [42]. The vibration of the PZT cantilever was performed by the fluttering of the wing. The study showed a power output of 2.2 mW at 8 ms^{-1} wind speed. Weinstein et al. used a PZT piezoelectric cantilever beam for energy harvesting in heating, ventilation, and air conditioning systems [43]. The beam's excitation was enhanced by an aerodynamic fin attached to its end, and the vortex shedding was caused by a bluff body (found ahead of the cantilever). The authors highlighted that by placing small weights along the fin, they were able to tune the piezoelectric device in order to function at resonance for flow velocities in the range of 2 to 5 ms^{-1}. The results showed that the output power was 3 mW for a wind speed of 5 ms^{-1}. Pan et al. developed an energy harvester with a right-angle cantilever beam structure [44]. Due to this specific configuration, the authors achieved significant improvement in the piezoelectric wind energy harvesting performance. The findings of the study indicated that the maximum output power of the right-angle cantilever beam was found to be over 1.3 mW at 6 ms^{-1} wind speed, with a load resistance of 500 kΩ. Such power output was twice as much as the traditional cantilever beam.

4. Energy Harvesting Applications

In their study, Zeibekis et al. investigated the optimization of the piezoelectric coefficients of polycrystalline $Pb(Zr_xTi_{1-x})O_3$ in order to achieve higher performance in energy harvesting applications [45]. To this effect, they focused on the influence of the sintering temperature (T_{sin}) on the piezoelectric properties of $Pb(Zr_{0.52}Ti_{0.48})O_3$. Furthermore, by employing an optical microscope-based local technique, they were able to record the strain (S_{zi} (i = x, y))–electric field ($E_{ex,z}$) hysteresis loops and hence, estimate both the piezoelectric coefficients (d_{zi} (i = x, y)) and the coercive field ($E_{C,i}$ (i = x, y)) [46,47].

Figure 7a,b illustrate the strain (S_{zi}^{tot} (i = x, y))–electric field ($E_{ex,z}$) data for $Pb(Zr_{0.52}Ti_{0.48})O_3$ sintered at T_{sin} = 1200 °C, varying the $E_{ex,z}$ from zero to ±9 $kVcm^{-1}$. The slope $d_{zi} = dS_{zi}^{tot}/dE_{ex,z}$ of the approximately linear parts of the loops provided the maximum d_{zi}. As indicated in Figure 7c, at T_{sin} = 1180 °C, d_{zi} was found to be 1080 pmV^{-1} along the X-symmetry axis of strain (SA_x) and 1120 pmV^{-1} along the Y-symmetry axis of strain (SA_y). Such a high value (d_{zi}~1100 pmV^{-1}) equals an increase of ~175% with respect to the baseline. Accordingly, for energy harvesting applications, the authors employed a bias electric field, E_{bias}, in such a way that the piezoelectric material is forced to operate at maximum d_{zi} for small fluctuations of the electric field. According to Figure 7d, a progressive increase in $E_{C,i}$ was recorded, reaching $E_{C,i}$~4.5–5.0 $kVcm^{-1}$ at T_{sin} = 1250 °C. Such a value corresponded to an increase in the order of 56% (44%) in SA_x (SA_y) [45].

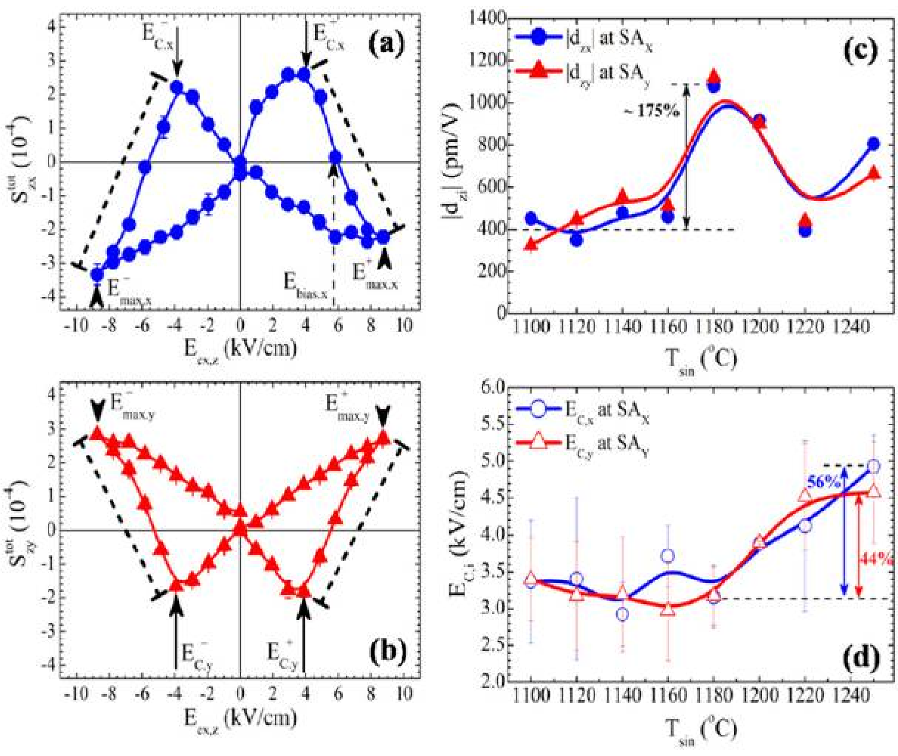

Figure 7. Strain (S_{zi}^{tot} (i = x, y))–electric field ($E_{ex,z}$) hysteresis loops for $Pb(Zr_{0.52}Ti_{0.48})O_3$ at T_{sin} = 1200 °C along the (**a**) X-symmetry axis of strain (SA_x) and (**b**) Y-symmetry axis of strain (SA_y). The $E_{ex,z}$ ranges from 0 to ±9 $kVcm^{-1}$. The term symmetry axis of strain, SA, highlights the expected direction of the sample's deformation in relation to its geometry. The coercive electric field, $E_{C,i}$, is illustrated by the solid vertical arrows, the maximum electric field, $E_{max,i}$, is indicated by the arrowheads, and the dashed lines show the approximately linear parts of the $S_{zi}^{tot}(E_{ex,z})$ loops, employed for the calculation of d_{zi}; (**c**) the variation of the piezoelectric coefficients, d_{zi} (i = x, y), and the (**d**) coercive electric field, $E_{C,i}$ (i = x, y), with the sintering temperature (T_{sin}) for the SA_x and SA_y (used with permission of IOP Publishing, from [45]; permission conveyed through Copyright Clearance Center, Inc., Danvers, MA, USA).

Figure 8 indicates the variation of mean grain size, GS, and density, ρ, of $Pb(Zr_{0.52}Ti_{0.48})O_3$ with respect to T_{sin}. The GS was increased from ~1.5 μm to ~4.5 μm for the interval 1100–1250 °C, in accordance with the respective values found in the literature. The density, ρ, was increased for the range 1100–1180 °C to the enhanced densification of $Pb(Zr_{0.52}Ti_{0.48})O_3$. For T_{sin} > 1180 °C, an abrupt decrease was recorded due to the possible mass losses in the sample [45].

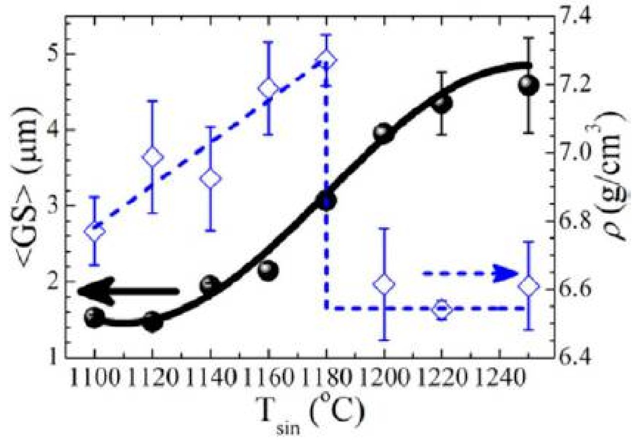

Figure 8. The dependence of the mean GS: spheres (left Y axis, as the thick arrow points) and density, ρ: rhombuses (right Y axis, as the dashed arrow points), of $Pb(Zr_{0.52}Ti_{0.48})O_3$ on T_{sin}. The fitting function of mean GS corresponds to the thick black solid line, while the one for ρ is the thin blue dashed line with respect to T_{sin} (used with permission of IOP Publishing, from [45]; permission conveyed through Copyright Clearance Center, Inc.).

Figure 9a shows XRD data of $Pb(Zr_{0.52}Ti_{0.48})O_3$ powder (starting material) and $Pb(Zr_{0.52}Ti_{0.48})O_3$ ceramics (processed samples) at various T_{sin} (1100–1250 °C). Figure 9b shows the broadening of the FWHM of the main peak (110) for T_{sin} > 1180 °C. Moreover, the significant shift of the peak (110) of $Pb(Zr_{0.52}Ti_{0.48})O_3$ samples sintered at T_{sin} > 1180 °C, shown in Figure 9c, constitutes a sign of compositional inhomogeneity. At T_{sin} < 1180 °C, the peak shows negligible shift, indicating that the homogeneity in the composition has been restored. Figure 9d shows that the peak (200) has been separated into two peaks, namely (002t) and (200t) at T_{sin} > 1180 °C. Such splitting is a characteristic behavior of the sintered $Pb(Zr_{0.52}Ti_{0.48})O_3$ samples to shift at the tetragonal phase of the MPB. The progressive splitting of the peak (2 1 1) at T_{sin} > 1180 °C (Figure 9e) was an indication of the formation of $PbTi_3O_7$ due to PbO losses upon increasing T_{sin} [45].

The authors concluded that such significantly high d_{zi}~1100 pmV^{-1} values found at T_{sin} = 1180 °C were motivated by the increase in the GS, while for higher temperatures, the values of d_{zi} deteriorated due to the existence of byproduct phases (i.e., $PbTi_3O_7$). Piezoelectric coefficients of ~1100 pmV^{-1} are remarkably higher than the ones found in the literature for PZT ceramics [45]. This result paves the way for the optimization of piezoelectric materials showing high coefficients for effective use in energy harvesting.

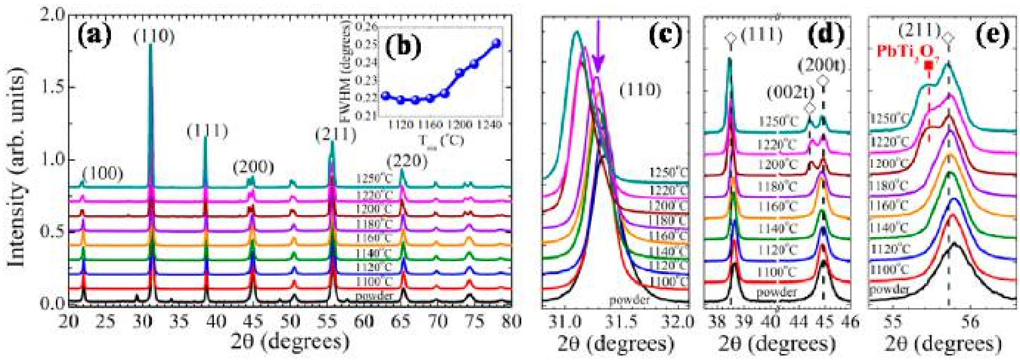

Figure 9. (**a**) XRD data of $Pb(Zr_{0.52}Ti_{0.48})O_3$ powder (starting material) and $Pb(Zr_{0.52}Ti_{0.48})O_3$ ceramics (processed samples) at various T_{sin} (1100–1250 °C). The peaks presented in the unsintered sample correspond to a-PbO_2, b-TiO_2, $PbTi_3O_7$, $Pb_2Ti_2O_6$, and $PbZrO_3$ oxides; (**b**) the full width at half maximum (FWHM) of the main peak (110) in relation to T_{sin}; (**c**) the main peak (110) shows a significant shift at T_{sin} > 1180 °C and a negligible shift at T_{sin} < 1180 °C; (**d**) the split of the peak (200) into well-separated peaks (002t) and (200t) gives evidence of the induced tetragonal phase at T_{sin} > 1180 °C. The peak (111) remains single. (**e**) The progressive splitting of the peak (211) at T_{sin} > 1180 °C evidences the formation of $PbTi_3O_7$ (used with permission of IOP Publishing, from [45]; permission conveyed through Copyright Clearance Center, Inc.).

Similarly, Vertsioti et al. studied the modulation of the piezoelectric coefficients for hybrid magnetoelectric samples, namely PZT-5%Fe_3O_4, of both square and disc shapes, under the presence of an external magnetic field applied along the z axis, $H_{ex,z}$ [48]. Concretely, they recorded the strain–electric field curve, $S(E_{ex,z})$, recorded upon application and removal of $H_{ex,z}$. To this effect, they employed an optical-microscopy-based local technique that enabled the authors to record the piezoelectric strain in any area of choice over the sample's surface, mainly focusing the investigation at the edges of the samples in order to capture the deformation in its full range. The obtained results are presented in the following Figures 10 and 11.

Figure 10(ai–ci,aii–cii) provide the strain (S_{zy})–electric field ($E_{ex,z}$) (denoted as solid rhombuses) loops for square-shaped and strain (S_{zx})–electric field ($E_{ex,z}$) (denoted as open rhombuses) loops for disc-shaped PZT-5%Fe_3O_4 samples of length/thickness 7 mm/0.4 mm and 6 mm/0.4 mm, respectively, in the absence (Loop index: 2), upon the application (Loop index: 4), and upon removal (Loop index: 6) of an externally applied magnetic field, $H_{ex,z}$ [48]. As shown, the loops that correspond to $S_{zx}(E_{ex,z})$ were horizontal lines due to the fact that the area under study was on the Y-symmetry axis (SA_y). Moreover, the application of $H_{ex,z}$ had an effect on the loops since, as is clearly illustrated, they became narrower (panels 10a(i,ii) vs. panels 10b(i,ii)). Upon removal of $H_{ex,z}$, they restored their original shape almost completely (panels 10a(i,ii) vs. panels 10c(i,ii)). The authors noted that the presence of $H_{ex,z}$ (1 kOe) caused a 50–60% decrease in the PE coefficient, d_{zy}, which was then recovered in the absence of $H_{ex,z}$ (Figure 11).

Furthermore, for the specific area under study (shown at the edge of both samples as a white dot in Figure 10), the recorded strain–electric field curves, $S(E_{ex,z})$, did not exhibit any noticeable difference for the differently shaped squares and discs, PZT-5%Fe_3O_4 samples, evidencing that the shape did not affect the data obtained in this case [48].

Figure 11 shows the mean value of the piezoelectric coefficient, $<|d_{zy}|>$, coming from the absolute values of the entire $S_{zy}(E_{ex,z})$ loop before applying (Loop index 1 and 2), upon application (Loop 3 and 4), and after removal (Loop index 5 and 6) of $H_{ex,z}$. The $<|d_{zy}|>$ was found by the slopes $|dS_{zy}/dE_{ex,z}|$ of the linear parts of $S_{zy}(E_{ex,z})$ [48]. The 50–60% decrease in $<|d_{zy}|>$ = 200–250 pm/V upon the presence of $H_{ex,z}$ = 1 kOe is plainly depicted.

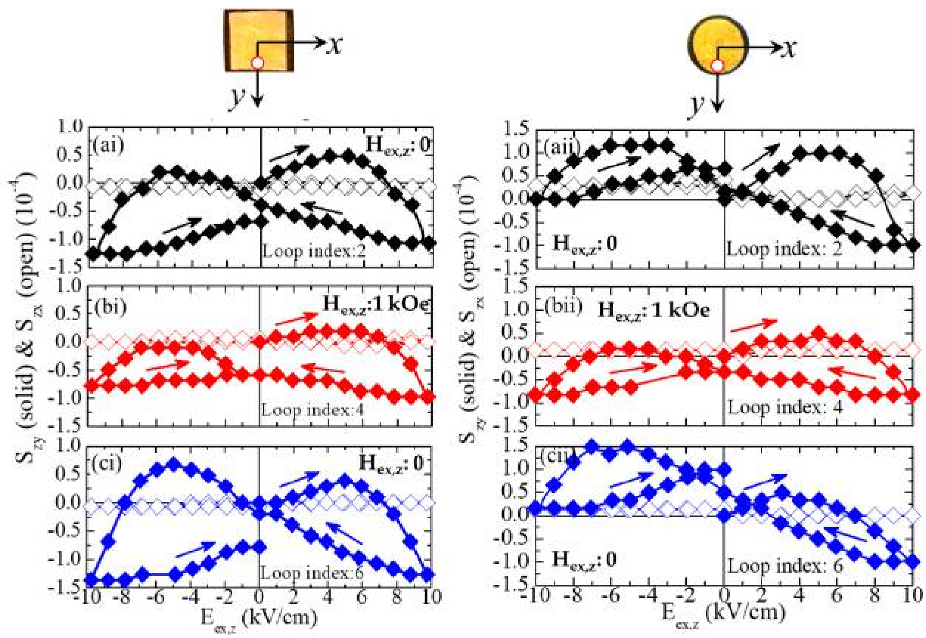

Figure 10. (**ai**–**ci**) Strain (S_{zy})–electric field ($E_{ex,z}$) (denoted as solid rhombuses) loops for square-shaped and (**aii**–**cii**) strain (S_{zx})–electric field ($E_{ex,z}$) (denoted as open rhombuses) loops for disc-shaped PZT-5%Fe_3O_4 samples of length/thickness 7 mm/0.4 mm and 6 mm/0.4 mm, respectively, in the absence (Loop index: 2), upon the application (Loop index: 4), and upon removal (Loop index: 6) of an externally applied magnetic field, $H_{ex,z}$. The arrows trace the sequence of $E_{ex,z}$ application. The respective samples, along with the arbitrarily chosen x and y coordinate system, are illustrated by the photos. The area under investigation is indicated with a dot placed on SA_y for both samples [48].

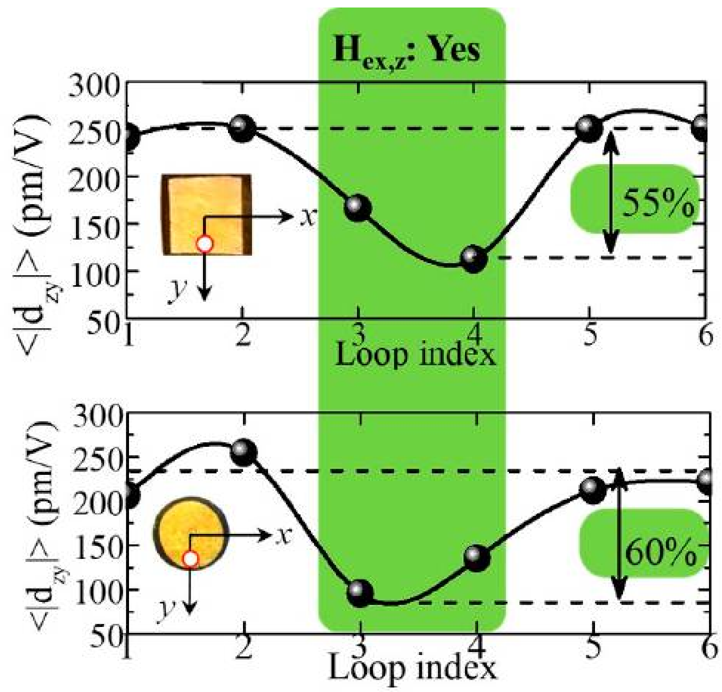

Figure 11. Mean value of piezoelectric coefficient, $<|d_{zy}|>$, coming from the absolute values of the entire $S_{zy}(E_{ex,z})$ loop as a function of an externally applied magnetic field, $H_{ex,z}$: in its absence (Loop index: 1 and 2), upon its application (Loop index: 3 and 4), and upon its removal (Loop index: 5 and 6). The respective samples, along with the arbitrarily selected x and y coordinates, are illustrated by the photos. The area under investigation is indicated with a dot placed on SA_y for both samples [48].

The authors concluded that the presence of Fe_3O_4 in PZT-5%Fe_3O_4 induces both static structural disorder and reconfigurable magnetic disorder that affect $S_{zy}(E_{ex,z})$ and PE data. The significant and reversible modulation of PE coefficients upon the presence/absence of $H_{ex,z}$ at room temperature renders the PZT-5%Fe_3O_4 a promising candidate for energy harvesting applications [48].

Energy harvesting from vibrations is an interesting mechanism for powering wireless sensors or devices exhibiting low power. In this case, a prerequisite is that the vibration energy harvesting device should be in resonance with the excitation frequency. For this reason, Challa et al. [49] proposed an approach in order to investigate the application of a magnetic force to modify the energy harvesting beam's stiffness, thereby allowing one to change the frequency of the transducer. The natural frequency of the beam was 26 Hz, which was successfully adjusted over a frequency range of 22–32 Hz, continuously providing a power output of 240–280 μW.

Chen et al. developed PZT nanofibers to serve as piezoelectric nanogenerators for mechanical energy harvesting [50]. The choice of nanofibers, instead of bulk or microfibers, was due to the fact that under electrospinning preparation, nanofibers exhibit extraordinary properties, including high piezoelectric voltage constant, high mechanical strength, and bending flexibility [51], hence rendering them potential candidates for the fabrication of highly efficient energy harvesting devices. The formation of the PZT nanofiber nanogenerator is schematically illustrated in Figure 12a. In brief, the PZT nanofibers were synthesized by electrospinning and then placed on interdigitated platinum fine-wire electrodes, which were constructed on a silicon-based substrate. The size characteristics of the obtained PZT nanofibers, namely diameter and length, were found to be 60 nm and 500 μm, respectively (Figure 12b). They were also embedded in a soft polydimethylsiloxane (PDMS) polymer in order to be protected from any potential damage (Figure 12c). The extraction electrodes served to connect the platinum fine-wire electrodes and transfer the electrons generated (by the nanofibers when subjected to stress) to an external circuit. As shown in Figure 12d, the nanofibers were polarized by subjecting them to an electric field (4 V/μm) between the electrodes for 24 h [50].

Figure 12e shows the generation mechanism of the power output of PZT nanofibers operating in longitudinal mode. The alternating pressure applied on the nanogenerator's surface was transferred through the polydimethylsiloxane (PDMS) polymer to the PZT nanofibers, ultimately producing charges owing to tensile and bending stresses. Thus, a voltage difference was formed between neighboring electrodes. The output power was enhanced by the interdigitated electrodes. The PZT nanofibers, which were laterally aligned on the interdigitated electrodes, served as unit cells between the electrodes connected in parallel. As mentioned above, when the nanofibers underwent external stresses, the respective generated electrons were transferred through the extraction electrodes. The vertical application of the stress to the PDMS could result in its transmission to the PZT nanofibers in the longitudinal direction [50].

Figure 13 shows the results of the measured voltage output versus strain (panel 13a) in the PDMS and of the power output versus the load resistance (panel 13b). Referring to panel 13a, the voltage output was increased by increasing the applied strain, with a maximum output of 1420 mV under ~7.5×10^{-5}% applied strain along the PZT nanofibers. Panel 13b shows the power delivered to the load by varying the load resistance from 0.1 to 10 MΩ under 10% applied strain on the surface of PDMS polymer and at a load frequency of 250 rad/s. The figure shows that the maximum recorded power was found to be 0.03 μW at 6 MΩ. The results showed that under the application of a periodic stress, the newly formed piezoelectric nanogenerator exhibited superior characteristics compared to the semiconductor type of piezoelectric nanowires and nanofibers, revealing an output voltage of 1420 V and a power of 0.03 μW [50].

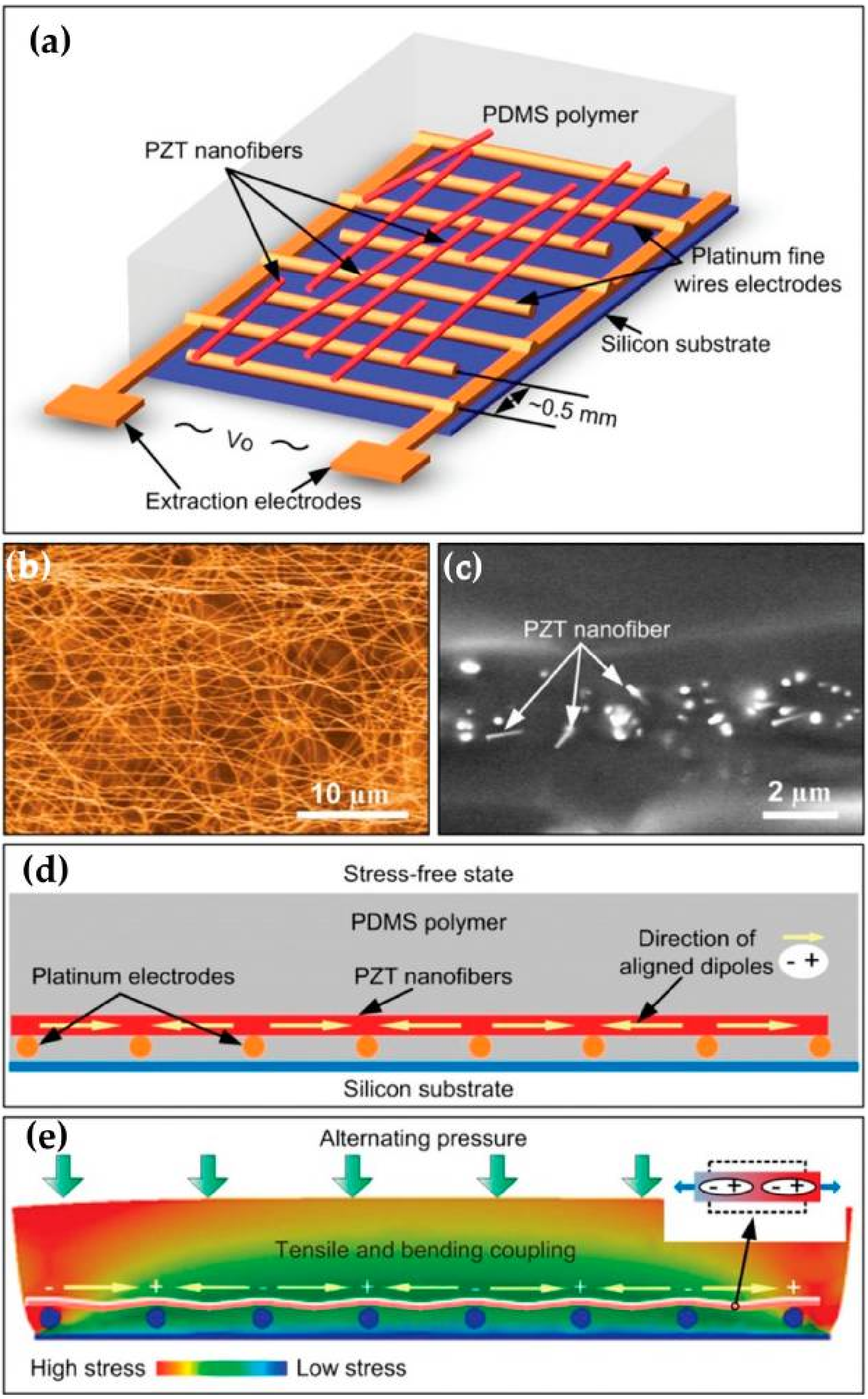

Figure 12. (**a**) Schematic illustration of PZT nanofiber (nano)generator; (**b**) representative scanning electron microscopy (SEM) image of PZT nanofibers deposited on platinum fine-wire electrodes; (**c**) SEM image of PZT nanofibers in the polydimethylsiloxane (PDMS) polymer; (**d**) cross-sectional illustration of PZT nanofibers, which were poled by an electric field of 4 V/μ across the electrodes; (**e**) power generation mechanism of PZT nanofibers working in longitudinal mode under the application of pressure on the top of the nanogenerator device. The color scale indicates the level of the stress owing to the applied pressure (reprinted with permission from Chen, X.; Xu, S.; Yao, N.; Shi, Y. 1.6 V nanogenerator for mechanical energy harvesting using PZT nanofibers. Nano Lett. 2010, 10, 2133. Copyright (2010) American Chemical Society).

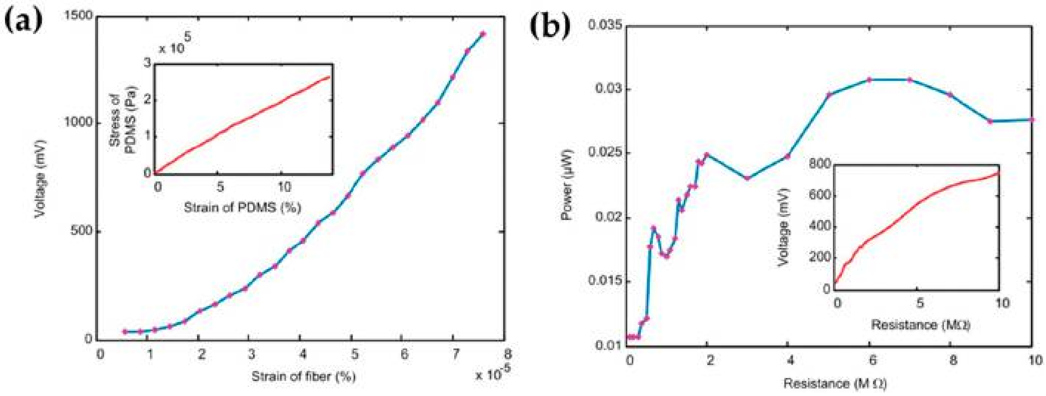

Figure 13. (**a**) The voltage output with respect to the strain of PZT nanofiber at ~39.8 Hz. The inset depicts the stress of composites in relation to the applied strain at the top and bottom of the surface of PDMS; (**b**) the power with respect to the load resistance. The inset indicates the output voltage in relation to the load resistance (reprinted with permission from Chen, X.; Xu, S.; Yao, N.; Shi, Y. 1.6 V nanogenerator for mechanical energy harvesting using PZT nanofibers. Nano Lett. 2010, 10, 2133. Copyright (2010) American Chemical Society).

Piezoelectric energy harvesting can be utilized in transportation for various purposes. In a study, the authors proposed a tracking wheel pressure technique to investigate the capacity of the road pavement to generate piezoelectricity. They show that an output voltage of 65 V and electric capacity of 0.8 kW/h were produced, leading to the effective powering of traffic signal lights [52]. In the study of Khalili et al., the development of a piezoelectric energy harvester was presented, which converted mechanical energy obtained from roadways into electricity [53]. Specifically, the aim was to scavenge the mechanical energy from roadways by employing a stack of parallel-combined piezoelectric generators. In the study, the authors used a single PZT stack at 66 Hz frequency and 500 kΩ external resistance to achieve voltages of 95 V and 1190 V, as well as power outputs of 9 mW and 1400 mW. Moreover, Gao et al. designed and tested a piezoelectric energy transducer [54]. In particular, the authors investigated a rail-borne energy harvester that exploited variations in rail acceleration. They simulated the rail system's conditions, and they achieved an output power of 4.9 mW and an output voltage of 22.1 V with a load impedance of 100 kΩ. Karimi et al. employed a piezoelectric energy harvester based on a cantilever beam to exploit vibrations caused by vehicles when traversing the bridge [55]. The authors show an output power of 35 µW, which was attributed to a 200 kΩ load resistance at the generator's resonance frequency of 13.5 Hz. It has been reported that the output of power of a single piezoelectric energy transducer is typically low when each vehicle transverses through a bridge [56]. Therefore, to overcome this issue, it is necessary to use multiple arrays of sensors under repeated traffic loading. It is well known that the existence of speed bumps on the roads serves to lower the vehicles' speed. In order to convert the kinetic energy produced by the vehicles when passing over a speed bump into electrical energy, piezoelectric energy harvesters should be embedded into the bumps for powering sensor nodes [57]. For this reason, in their study, Chen et al. developed an impact-induced vibration piezoelectric cantilever for converting the mechanical vibration energy into AC electrical power and a low-power management circuit for collecting the electrical power in order to provide a system for energy harvesting for speed bumps [57]. The efficiency of the system was found to be 74%. Furthermore, 1.26 mJ was produced by a single cantilever when one vehicle was passing over the bump; 0.82 mJ of the energy was used to power the battery when the circuit's sleep mode was operated, while in the opposite case, the energy was consumed within 25 s. Accordingly, the circuit's sleep mode was crucial for reducing energy losses and increasing the effectiveness of the energy harvester. Moreover, converting the mechanical energy coming from the tires, engine, and suspensions into electrical energy by using energy harvesters could result in the effective powering of wireless sensors, thus improving the overall functionality of the cars and reducing their costs in both economic and environmental terms. It has been reported that torsional vibration generated from combustion engines can be harvested in order to provide electrical energy for a wireless sensor node system [58]. Briefly, the piezoelectric energy harvester was created by mounting a cantilever beam on the surface of the rotating shaft. This enabled the production of a power of 14 µW to potentially power wireless shaft torque transducers at an engine speed of 2000 rpm. In order to power a system that monitors the tires' pressure, Esmaeeli et al. developed a rainbow piezoelectric energy harvester, which they placed inside a pneumatic tire [59]. The efficiency of the rainbow system was found to be 0.69%, hence resolving the problems associated with the use of batteries for powering tire pressure sensors.

To achieve wind energy harvesting, Phan et al. developed triboelectric nanogenerators (TENGs) consisting of a parallel structure of two electrodes, a top and a bottom, with a flutter membrane in between, which served as an airflow energy harvester (Figure 14) [60]. The TENGs were able to produce triboelectricity, converting the mechanical interactions caused by the airflow on the membrane. Each unit component of the flutter membrane featured a thin AI foil electrode. The electrode was covered on both sides with nanofiber-shaped mats made of electrospun poly(vinyl chloride) (PVC). Under mild airflow, the provided power output from a single unit of the flutter-based TENGs was found to be 0.33 µW. In order to enhance the output performance of the harvester, the authors fabricated a multi-layered TENG. This was achieved by multiple stacking single units. In addition, to improve the electric outputs, the authors mounted a rubber belt between the flutter membranes, as indicated in Figure 14. The presence of the flutter-rubber belt facilitated the instantaneous triboelectrification between the flutter membrane and the electrode. This occurred due to the vigorous vibration of the rubber belt when the airflow entered the nanogenerator, which synergistically combined the aerodynamic and aeroelastic movement of the membrane. The authors highlighted that the aerodynamic and aeroelastic flutter-driven TENGs showed great potential to create sustainable and cost-efficient wind energy harvesting systems, as well as to be employed in various applications, such as wireless sensor applications for automobiles or aircraft.

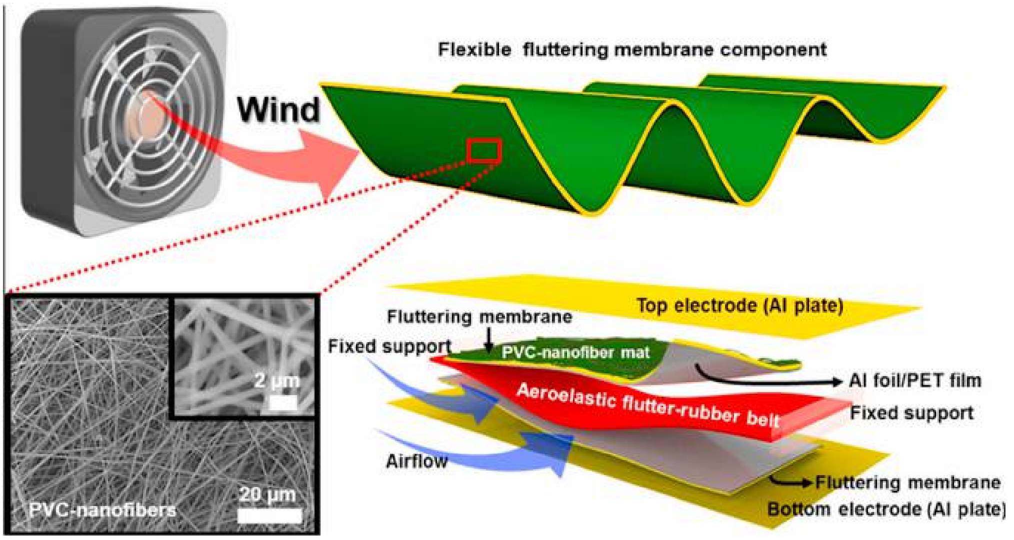

Figure 14. Wind energy harvesting is achieved by employing flutter-propelled aerodynamic and aeroelastic triboelectric nanogenerators (TENGs) (reprinted from [60], copyright (2017), with permission from Elsevier).

Wu et al. developed a wind energy harvester, which consisted of a cantilever attached to piezoelectric patches and a proof mass [61]. By exploiting the vibration of the piezoelectric cantilever induced by the crosswind, they show that the electric power output was 2 W by manipulating the resonant frequency of the cantilever. Furthermore, the study indicated that for a crosswind velocity of 9–10 ms^{-1}, the generated electric power output was found to be up to 1.02 W, leading to an efficient wind energy harvesting device.

In another study, inverted piezoelectric flags were developed for wind energy harvesting that exhibited sustained power generation (∼0.4 mW/cm^3), even in the low wind-speed range (3.5 m/s), and the resonance was adjusted by modifying the bending stiffness of the flag (the self-fluttering does not depend on resonance) [62]. Also, by adjusting the flag's length, the inverted flag configuration was tuned to self-oscillate at a desired wind speed. The controlled wind experiments indicated power outputs of 1–5 mW/cm^3 and 0.1–0.4 mW/cm^3 for wind speeds of 5–9 m/s and 2.5–4.5 m/s, respectively, using flags with 60 mm length in the former case and 100 mm length in the latter case. Additionally, outdoor experiments were conducted to investigate the performance of the inverted piezoelectric flag under natural and non-uniform wind conditions. The harvested ambient wind energy was employed to power a digital temperature sensor without storing electricity. The experimental setup is illustrated in Figure 15. As shown, the piezoelectric flag consisted of ten poled PVDF membranes, ultimately exhibiting final dimensions of 100 × 200 × 0.2 mm^3. The flag was mounted on a stainless-steel tripod, which was fixed on a wood sheet. Wind sensors were also connected in the tripod in order to provide appropriate data concerning the speed and direction of the wind. Moreover, a self-alignment mechanism was incorporated in order to align the flag with respect to the direction of the wind.

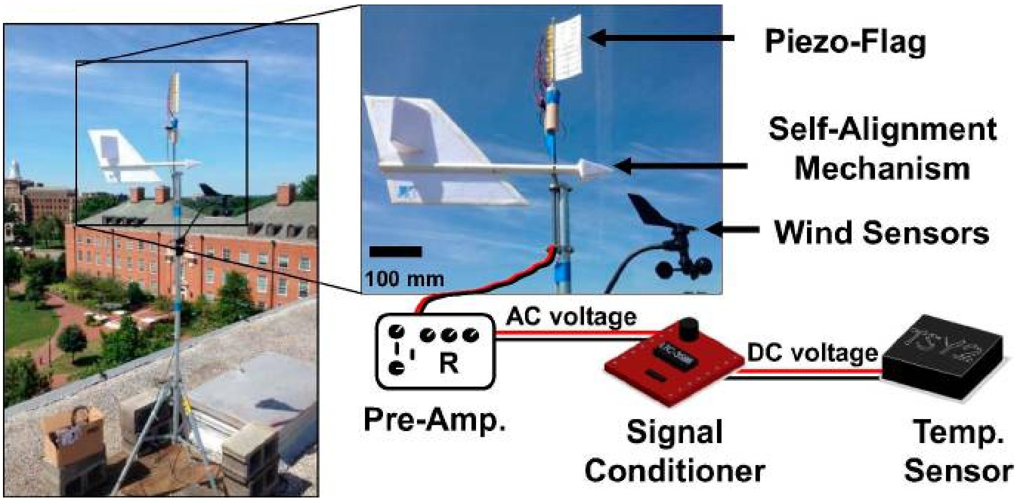

Figure 15. Energy harvesting experimental configuration. The piezoelectric flag was employed to power a digital temperature sensor utilizing ambient wind energy. The input voltage was provided by both a pre-amplifier and a signal conditioner to the temperature sensor. The inset photo shows the self-alignment mechanism of the piezoelectric flag with respect to wind direction (reprinted from [62], copyright (2017), with permission from Elsevier).

According to Figure 16, during the operation of the sensor, one temperature value was provided by simply calculating the mean value of five consecutive peaks of the output signal (shown as On). This criterion was set by the authors since the magnitude of the input voltage has the tendency to fluctuate according to the flag's flapping behavior and energy generation. Thus, the output signal of the sensor will fluctuate as well. The results showed that the normal operation of the temperature sensor was not affected by the wind fluctuations found in the outdoor environment. Concretely, thanks to the self-alignment mechanism, the sensor operated successfully, namely 1.5 times/min and one time every 10 min during the day and night, respectively, leading to a more than 20-fold increase in the sensor data output [62].

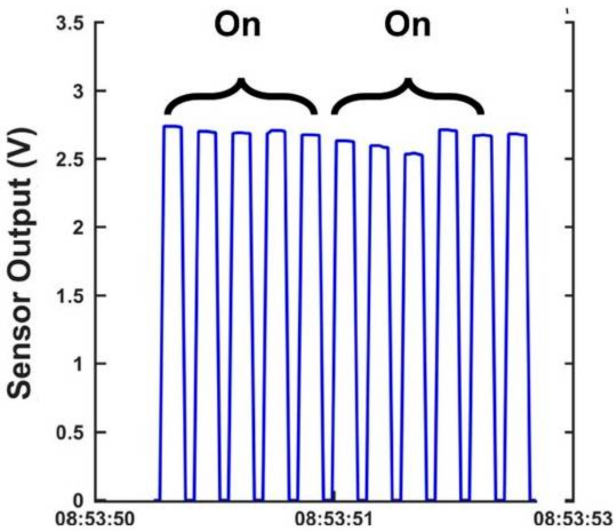

Figure 16. The output signal of the sensor that is used to determine the temperature of the air. The mean value of five consecutive peaks of the output signal (shown as On) was used to calculate one temperature value. Each five-peak range indicated that the sensor operated successfully, while a peak range of less than five peaks indicated that the sensor did not operate in this range (reprinted from [62], copyright (2017), with permission from Elsevier).

Hwang et al. proposed a piezoelectric energy harvester that can be employed to exploit the ocean's energy [63]. The authors developed a system that consisted of a piezoelectric cantilever, in which a magnet was attached as tip-mass. A rail with a metal ball was placed on top of the magnet. Their findings showed that the proposed harvester can be employed in low-frequency vibration applications, such as those induced by ocean waves and in sea-based applications involving buoys and boats. Viet et al. investigated the use of a floating energy harvester employing the piezoelectric effect in order to harvest energy from intermediate and deep waves [64]. The findings showed that for a floating energy harvester having 1 m width, 0.5 m height, 1 m length, 100 kg mass of the mass-spring, and a sea wave with 2 m amplitude and 6 s period, up to 103 W of power can be harvested.

Natural human body activities (such as heart beating, breathing, walking, joint movements, etc.) constitute significant energy sources for powering piezoelectric wearable devices. Jung et al. demonstrated a curved piezoelectric generator applicable in wearable mechanisms, producing high power output [65]. Since human motion is characterized by its low frequency and its respected large displacements, the authors used the flexible polymer PVDF integrated on the curved polyimide (PI) platform to develop the wearable energy harvester in order to easily exploit such mechanical energy. Specifically, the curved piezoelectric generator consisted of two connected back-to-back curved piezoelectric generators, where each one contained a PI substrate and two piezoelectric materials made of PVDF. Electrodes were also attached on the top and bottom sides of the PI substrate of the one piezoelectric generator, which used the 31-mode of operation (see Figure 2b). Furthermore, the curved structure enabled the increase in the output power production, as well as the operation at low-frequency vibration ranges. According to the findings of the study, 476 LED bulbs were powered since the harvester provided an output power density of 3.9 mW/cm^2. At low frequencies (<50 Hz), an output power and output current of ~55 V and ~250 μA, respectively, were generated due to the curved structure of the generator. The authors also investigated its potential as a wearable device in shoe-insole applications. Figure 17a illustrates the curved piezoelectric generator (7 × 4 cm^2) embedded into a shoe's insole. Figure 17b–e demonstrate the output voltage (panels 17b,d) and output current (panels 17c,e) of the curved piezoelectric generator, shown in panel 17a, during walking and running by a 68 kg human, respectively. The output signals presented were rectified by using a full-wave bridge diode chip. As indicated, an average output voltage of ~25 V and an average output current of ~20 µA were recorded during walking at low frequency (0.5 Hz). Similarly, an average output voltage of ~40 V and an average output current of ~47 µA were recorded during running. The authors highlighted that this finding would be useful for LED lighting during walking at night, which is beneficial for the safety of humans and for transmitting RF data for the purpose of working out. Overall, the authors concluded that the results of this study lay the foundations for the application of wearable technology based on piezoelectric materials in harvesting energy from physical human activities.

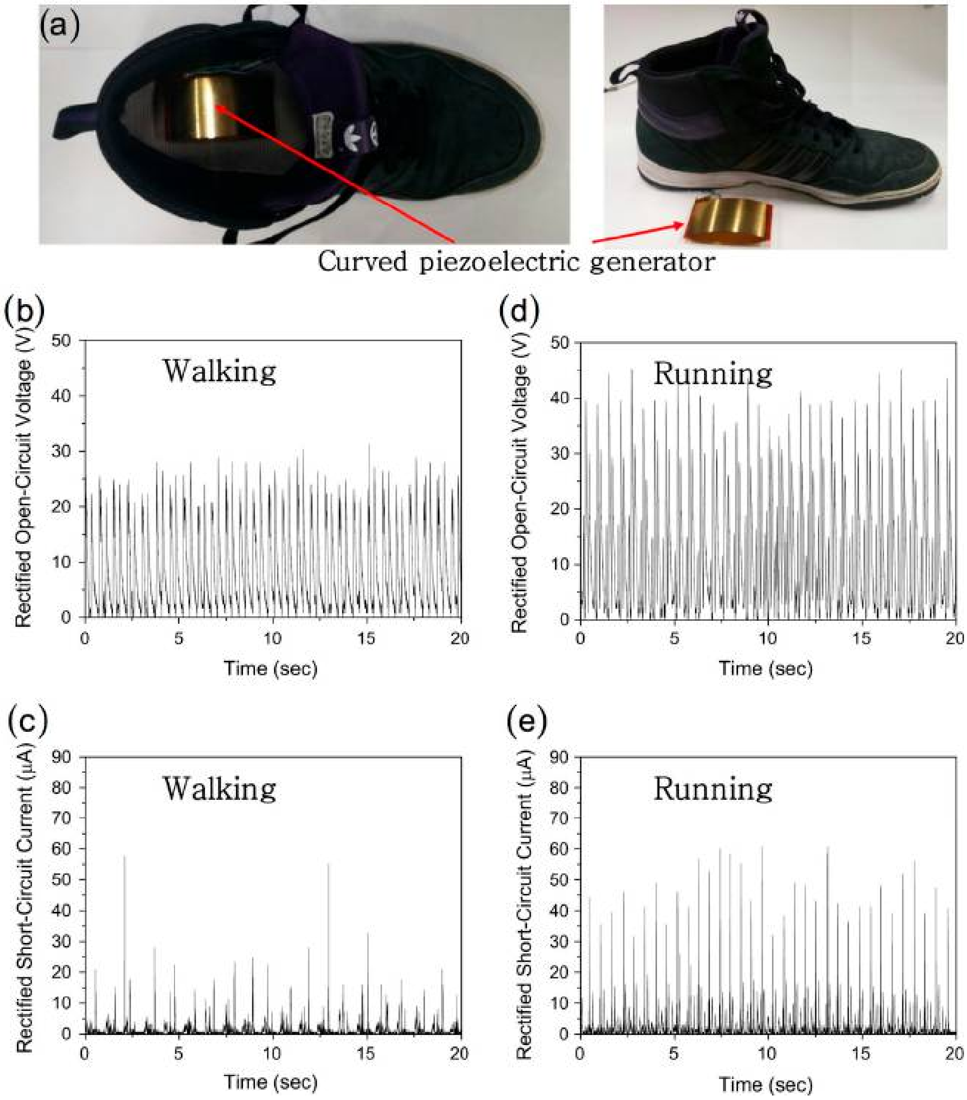

Figure 17. (**a**) Curved piezoelectric generator (7 × 4 cm^2) for shoe-insole application; output voltage (**b**,**d**) and output current (**c**,**e**) of the curved piezoelectric generator embedded into the insole during walking and running, respectively (reprinted from [65], copyright (2015), with permission from Elsevier).

Fan et al. developed a piezoelectric energy harvester whose main components were a piezoelectric cantilever beam, a magnetically coupled ferromagnetic ball, and a crossbeam in order to harvest energy produced by foot activities (such as vibrations, swing, and compressive force) [66]. The authors show that during a gait cycle, 0.03 mW to 0.35 mW was generated when the walking velocity ranged from 2 to 8 Km/h, yielding an improved performance of the proposed piezoelectric energy harvester compared to conventional ones. Li et al. synthesized a wearable energy harvester comprising a micro-electroplated nickel ferromagnetic cantilever and a magnet, and each one was bonded on a flexible substrate [67].

The purpose of the study was to create a piezoelectric energy harvester that uses the elbow joint to produce electrical energy. The results indicated that resonance up to hundreds of Hz was produced by the ultra-low-frequency limb motions that were made by the joint rotation upon a release and pull cycle. At the highest level of movement conditions, a voltage of 7.5 V and a maximum output power of 0.457 μW were achieved. Shi et al. introduced a piezoelectric energy harvester based on dual piezoelectric–electromagnetic coupling for capturing the swinging motion of the human arm [68]. Referring to the piezoelectric unit, the harvester comprised two PZTs, while the electromagnetic unit included a pair of arc-shaped drive magnets and two sets of coils. The drive magnets served to couple the two units, and along with the coils, they generated electrical energy and triggered the two PZTs, leading to the up-conversion of their frequency. The results of the study showed that due to its dual-modality character, the piezoelectric energy harvester improved its effectiveness by approximately 23 times, providing an output power enhancement of 2.754%. It could power electronic devices, highlighting its potential in energy harvesting from human motion.

Powering implantable medical devices through piezoelectric energy harvesting paves the way for developing sustainable and self-powered devices that reduce the patients' physical/psychological pain and associated financial problems, leading to the overall improvement in the quality of their lives. For example, Kim et al. investigated the powering of cardiac sensors by in vivo piezoelectric energy harvesters [69]. Specifically, the authors designed a biocompatible and flexible single-crystalline generator based on $(1-x)Pb(Mg_{1/3}Nb_{2/3})O_3-xPb(Zr,Ti)O_3$ (or PMN-PZT). The energy harvester demonstrated an output voltage of 17.8 V and a current of 1.75 μA from the porcine heartbeats, resulting in its potential use in biomedical applications. Dagdeviren et al. developed a thin-film PZT nanoribbon-based piezoelectric nanogenerator for biochemical energy harvesting from the movement of the heart and lungs in vivo [70]. Both a bridge rectifier and a micro battery were incorporated with the PZT harvester on a flexible substrate, and the whole device was encapsulated by a biocompatible layer for in vivo application. When the piezoelectric nanogenerator was coupled to the heart's right ventricle, the open-circuit voltage reached up to 5 V and was three orders of magnitude higher than in earlier in vivo studies.

Hwang et al. developed a piezoelectric nanogenerator device by using single-crystalline PMN-PT thin film (with 2500 pC/N) in order to supply an artificial cardiac pacemaker with electrical energy [71]. Figure 18(a(i)–a(iv)) show in detail the construction and application test of the device on the living heart of a rat. Initially, single-crystalline rhombohedral 0.72 PMT–0.28 PT was developed close to MPB, in this way obtaining high piezoelectric and electromechanical coupling coefficients. PMN-PT crystal was cut into a square block and placed on a bottom Au electrode. By using adhesive epoxy, the bottom Au electrode was bonded to a silicon wafer. The PMN-PT plate was formed into a film of 8.4 μm thickness and was then poled by applying an electric field of 1.8 kV/mm for 1 h. Afterwards, an Au electrode was deposited into the top surface of the PMN-PT thin film. By employing an electroplated tensile Ni stressor, the top piezoelectric portion of the PMN-PT metal-insulator-metal (MIM) was peeled off. The directional stress mismatch between the top Ni film and the underlying layers of the MIM/epoxy/wafer was used to effectively exfoliate the thin film without any damage. Additionally, the thickness of the exfoliated PMN-PT could easily be adjusted by altering the residual stress in the Ni film and a 20 μm thick Ni layer being the optimal condition for the safe detachment of the MIM structure. The PMN-PT was transferred onto a polyethylene terephthalate (PET) substrate in order to achieve conformal contact on a curved subcutaneous layer and corrugated organs in the human body. Cu wires were connected with stimulation electrodes to stimulate the rat's heart. Finally, the PMN-PT stimulator was ultimately used as an artificial pacemaker by generating electrical energy through the periodic bending and unbending of the device. Figure 18b indicates a cross-sectional SEM image of the PMN-PT thin film on the PET substrate. The inset exhibits XRD data of the PMN-PT thin film, confirming the synthesis of a pure perovskite. Figure 18c indicates the Raman spectroscopy data of PMN-PT thin film, which are consistent with the typical features for perovskite relaxors. Figure 18d shows the EDS spectrum and elemental mapping analysis of PMN-PT thin film. Figure 18e demonstrates the flexible PMN-PT energy harvester being fully bent by tweezers without any significant damage. The inset illustrates the device on a rounded-shape glass vial of 1.4 cm radius. The Ni-exfoliated PMN-PT on a plastic substrate offers exceptional bendability and stability to nanogenerators.

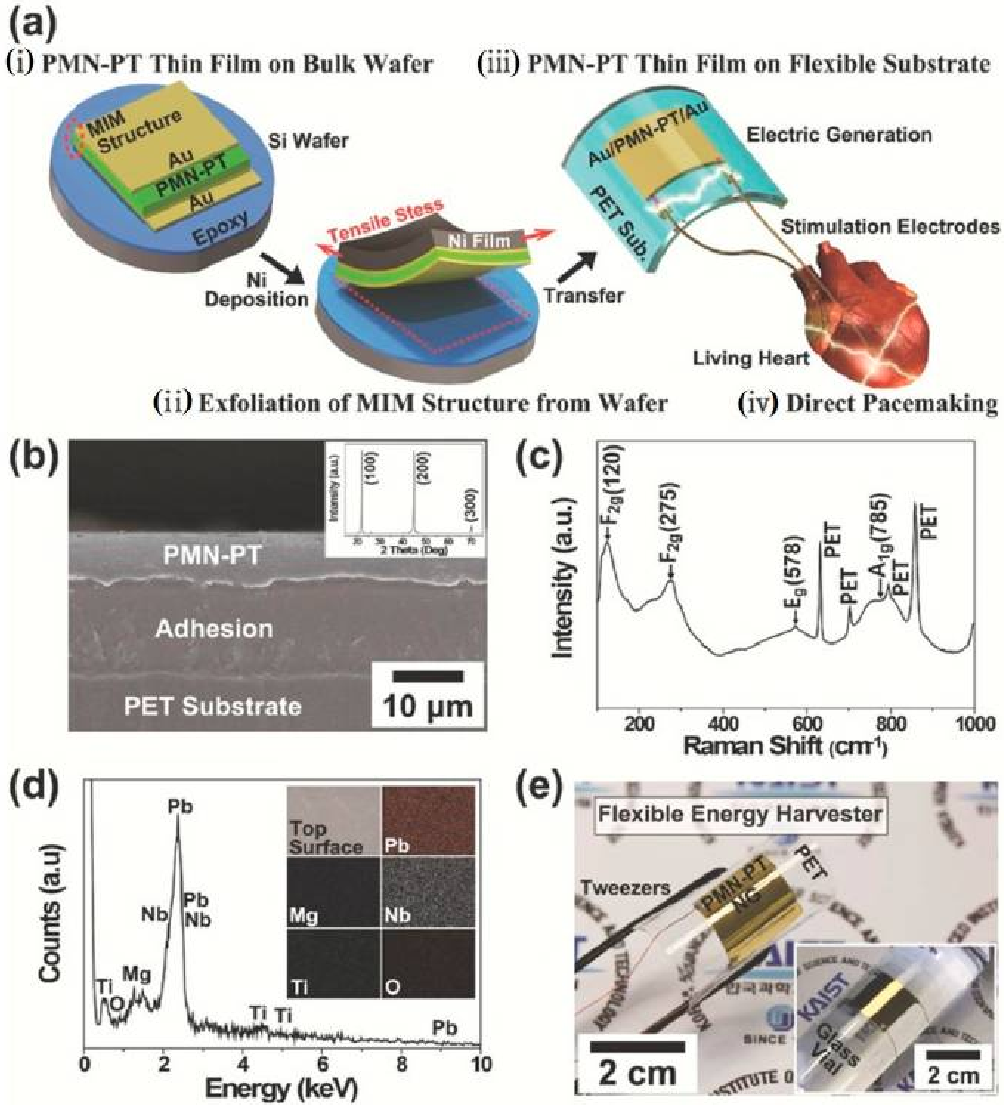

Figure 18. (**a**(**i**)–**a**(**iv**)) Synthesis of PMN-PT piezoelectric energy harvester for biomedical application; (**b**) a representative cross-sectional SEM image of PMN-PT thin film on a polyethylene terephthalate (PET) substrate. The inset shows XRD data of PMN-PT thin film confirming the synthesis of a pure perovskite; (**c**) the obtained Raman spectroscopy data of PMN-PT thin film were found to be in accordance with the typical features for perovskite relaxors; (**d**) EDS spectrum and elemental mapping analysis (shown in the respective inset) of PMN-PT; (**e**) PMN-PT thin film on a PET substrate completely bent by tweezers. The inset illustrates the device on a rounded-shape glass vial of 1.4 cm radius (copyright (2014) Wiley; used with permission from [71]).

Figure 19a demonstrates the functional electrical stimulation of the artificial cardiac pacemaker using the PMN-PT (thin film) energy harvester. As illustrated, the PMN-PT thin-film stimulator provided electrical stimuli to the heart through stimulation electrodes, while the electrocardiogram (ECG) of the anesthetized rat was simultaneously being recorded. The heart was stimulated during an open-heart operation. Figure 19c shows the rat's ECG before stimulation with the pacemaker, with a heart rate of six beats per second. The inset indicates the form of its heartbeat, which consists of the typical QRS complex and P and T waves. The periodic bending and unbending of the PMN-PT stimulator was apparent due to the appearance of spike peaks on the rat's ECG (Figure 19d). Provided that one bending motion of the stimulator generated 2.7 μJ of electric energy, the heart was significantly stimulated since this amount of energy was higher than the threshold energy (1.1 μJ) needed to electrically trigger the living heart.

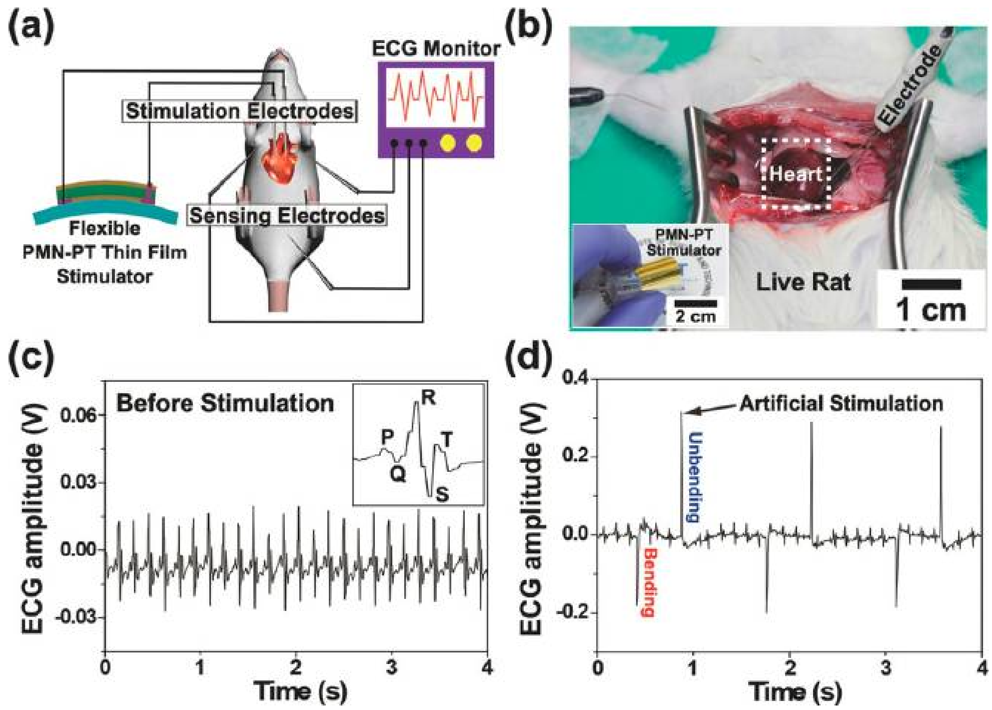

Figure 19. (**a**) Schematic illustration of the utilization of the PMN-PT energy harvester in a practical demonstration of a self-powered cardiac pacemaker; (**b**) the PMN-PT thin film is used to stimulate the heart of a live rat during open-heart surgery; (**c**) the obtained ECG before stimulation with the pacemaker. The inset indicates the form of the rat's heartbeat, which consists of the typical QRS complex and P and T waves; (**d**) the appearance of the peaks on the ECG was due to the stimulation of the heart after cyclical bending and unbending of the PMN-PT energy harvester (copyright (2014) Wiley; used with permission from [71]).

Zhang et al. designed a piezoelectric nanogenerator for enhancing osteogenesis in MC3T3-E1 cells by employing a novel thermoforming process [72]. The results of the study showed that the piezoelectric nanogenerator stimulated MC3T3-E1 cell proliferation and an increase in intracellular calcium ions, rendering it a successful candidate for bone repair. Du et al. synthesized a bioinspired hybrid patch with a self-adhesive and piezoelectric nanogenerator for healing wounds on the skin [73]. Their findings demonstrated that the patch could be used as a real-time electrical stimulation device since it promoted in vitro fibroblast proliferation, in vivo collagen deposition, and angiogenesis and significantly reduced by one-third the wound closure time, facilitating quicker healing of the wound. Furthermore, drug delivery using piezoelectric energy harvesters has attracted significant attention due to their succinct motion and therapeutic effectiveness [74,75].

5. Conclusions

The use of piezoelectric and ferroelectric materials in energy harvesting applications has received significant attention due to their unique physical properties that are being harnessed to develop efficient and sustainable energy harvesting devices. These materials are unique thanks to their ability to transform mechanical energy into electrical through a relatively simple physical mechanism: the application of mechanical stress to a piezoelectric material alters the spontaneous polarization so that bound charges become free to move through an external circuit, ultimately allowing the direct generation of a piezoelectric current. The conversion of usable electrical energy in response to a mechanical stress is beneficial for the general context of the growing demand for renewable and clean energy, the need to mitigate the environmental impact of energy production, and to remove the limitations posed by traditional batteries. Among the various piezoelectric materials under study, PZT ceramics and PMN-PT single crystals are the most commonly used. On one hand, PZT is the reference compound in polycrystalline materials due to its easy methods of production, good piezoelectric properties, and low cost. On the other hand, the more complicated PMN-PT is the compound of choice for single crystals thanks to its higher piezoelectric performance. Consequently, the present work provided a review of the physical properties of piezoelectric and ferroelectric materials, along with a description of their current application in energy harvesting technology. Specifically, we focused on PZT and PMN-PT and revealed the connection between their physical properties and their performance in various applications of energy harvesting. Continuous research on piezoelectric and ferroelectric materials paves the way for the development and optimization (i.e., minimization of energy conversion losses, maximization of efficiency, etc.) of new energy harvesting devices that exploit various energy sources, i.e., from different kinds of vibrations that stem from transportation, wind, water, and human motion, since all these are significant candidates that can effortlessly refill our reservoirs of electrical energy.

Author Contributions: Writing—original draft preparation, M.-A.K. and D.S.; writing—review and editing, M.-A.K., K.T., and D.S. All authors have read and agreed to the published version of the manuscript.

Funding: Hellenic Foundation for Research and Innovation, Basic Research Financing (Horizontal support for all Sciences), National Recovery and Resilience Plan (Greece 2.0).

Data Availability Statement: Not applicable.

Acknowledgments: M. A. Karageorgou and K. L. Tsakmakidis acknowledge funding within the framework of the National Recovery and Resilience Plan Greece 2.0, funded by the European Union–NextGenerationEU (Implementation body: HFRI), under Grant No. 16909. K. L. Tsakmakidis was also supported by the General Secretariat for Research and Technology and the Hellenic Foundation for Research and Innovation under Grant No. 4509.

Conflicts of Interest: The authors declare no conflicts of interest.

References

1. Maghsoudi Nia, E.; Wan Abdullah Zawawi, N.A.; Mahinder Singh, B.S. Design of a pavement using piezoelectric materials. *Mater. Werkst.* **2019**, *50*, 320–328. [CrossRef]
2. Sezer, N.; Koç, M. A comprehensive review on the state-of-the-art of piezoelectric energy harvesting. *Nano Energy* **2021**, *80*, 105567. [CrossRef]
3. Chen, J.; Oh, S.K.; Nabulsi, N.; Johnson, H.; Wang, W.; Ryou, J.-H. Biocompatible and sustainable power supply for self-powered wearable and implantable electronics using iii-nitride thin-film-based flexible piezoelectric generator. *Nano Energy* **2019**, *57*, 670–679. [CrossRef]
4. Kim, H.S.; Kim, J.-H.; Kim, J. A review of piezoelectric energy harvesting based on vibration. *Int. J. Precis. Eng. Man.* **2011**, *12*, 1129–1141. [CrossRef]
5. Covaci, C.; Gontean, A. Piezoelectric energy harvesting solutions: A review. *Sensors* **2020**, *20*, 3512. [CrossRef] [PubMed]
6. Wang, X. A study of harvested power and energy harvesting efficiency using frequency response analyses of power variables. *Mech. Syst. Signal Process.* **2019**, *133*, 106277. [CrossRef]
7. Cho, J.Y.; Kim, K.B.; Hwang, W.S.; Yang, C.H.; Ahn, J.H.; Hong, S.D.; Sung, T.H. A multifunctional road-compatible piezoelectric energy harvester for autonomous driver-assist LED indicators with a self-monitoring system. *Appl. Energy* **2019**, *242*, 294–301. [CrossRef]
8. Wang, Y.; Zang, P.; Yang, D.; Zhang, R.; Gai, S.; Yang, P. The fundamentals and applications of piezoelectric materials for tumor therapy: Recent advances and outlook. *Mater. Horiz.* **2023**, *10*, 1140. [CrossRef]
9. Kholkin, A.L.; Pertsev, N.A.; Goltsev, A.V. Piezoelectricity and Crystal Symmetry. In *Piezoelectric and Acoustic Materials for Transducer Applications*; Safari, A., Akdoğan, E.K., Eds.; Springer: Boston, MA, USA, 2008; pp. 17–38.

10. Soin, N.; Anand, S.C.; Shah, T.H. Energy Harvesting and storage textiles. In *Handbook of Technical Textiles*, 2nd ed.; Horrocks, A.R., Anand, S.C., Eds.; Elsevier: Amsterdam, The Netherlands, 2016; Volume 2, pp. 357–396.
11. Jain, A.; Prashanth, K.J.; Sharma, A.K.; Jain, A.; Rashmi, P.N. Dielectric and piezoelectric properties of pvdf/pzt composites: A review. *Polym. Eng. Sci.* **2015**, *55*, 1589–1616. [CrossRef]
12. Briscoe, J.; Dunn, S. 2.1 Background. In *Nanostructured Piezoelectric Energy Harvesters*, 1st ed.; Springer International Publishing: Berlin/Heidelberg, Germany, 2014; pp. 3–4.
13. Li, H.; Bowen, C.R.; Yang, Y. Scavenging Energy Sources Using Ferroelectric Materials. *Adv. Funct. Mater.* **2021**, *31*, 2100905. [CrossRef]
14. Deutz, D.B.; Pascoe, J.-A.; Schelen, B.; Van Der Zwaag, S.; De Leeuw, D.M.; Groen, P. Analysis and experimental validation of the figure of merit for piezoelectric energy harvesters. *Mater. Horiz.* **2018**, *5*, 444–453. [CrossRef]
15. Siang, M.L.; Leong, M.S. Review of vibration-based energy harvesting technology: Mechanism and architectural approach. *Int. J. Energy Res.* **2018**, *42*, 1866–1893. [CrossRef]
16. Wei, H.; Wang, H.; Xia, Y.; Cui, D.; Shi, Y.; Dong, M.; Liu, C.; Ding, T.; Zhang, J.; Ma, Y.; et al. An overview of lead-free piezoelectric materials and devices. *J. Mater. Chem. C* **2018**, *6*, 12446–12467. [CrossRef]
17. Li, H.; Tian, C.; Deng, Z.D. Energy harvesting from low frequency applications using piezoelectric materials. *Appl. Phys. Rev.* **2014**, *1*, 041301. [CrossRef]
18. Roundy, S.; Wright, P.K.; Rabaey, J. A study of low level vibrations as a power source for wireless sensor nodes. *Comput. Commun.* **2003**, *26*, 1131–1144. [CrossRef]
19. Wei, X.K.; Domingo, N.; Sun, Y.; Balke, N.; Dunin-Borkowski, R.E.; Mayer, J. Progress on Emerging Ferroelectric Materials for Energy Harvesting, Storage and Conversion. *Adv. Energy Mater.* **2022**, *12*, 2201199. [CrossRef]
20. Damjanovic, D. Ferroelectric, dielectric and piezoelectric properties of ferroelectric thin films and ceramics. *Rep. Prog. Phys.* **1998**, *61*, 1267–1324. [CrossRef]
21. Fousek, J.; Janovec, V. The Orientation of Domain Walls in Twinned Ferroelectric Crystals. *J. Appl. Phys.* **1969**, *40*, 135–142. [CrossRef]
22. Fang, H. Introduction. In *Novel Devices Based on Relaxor Ferroelectric PMN-PT Single Crystals*; Springer: Singapore, 2020; pp. 1–28.
23. Jin, L.; Li, F.; Zhang, S. Decoding the Fingerprint of Ferroelectric Loops: Comprehension of the Material Properties and Structures. *J. Am. Ceram. Soc.* **2014**, *97*, 1–27. [CrossRef]
24. Viola, G.; Saunders, T.; Wei, X.; Chong, K.B.; Luo, H.; Reece, M.J.; Yan, H. Contribution of piezoelectric effect, electrostriction and ferroelectric/ferroelastic switching to strain-electric field response of dielectrics. *J. Adv. Dielectr.* **2013**, *3*, 1350007. [CrossRef]
25. Priya, S. Advances in energy harvesting using low profile piezoelectric transducers. *J. Electroceram.* **2007**, *19*, 165–182. [CrossRef]
26. Kungl, H.; Fett, T.; Wagner, S.; Hoffmann, M.J. Nonlinearity of strain and strain hysteresis in morphotropic LaSr-doped lead zirconate titanate under unipolar cycling with high electric fields. *J. Appl. Phys.* **2007**, *101*, 044101. [CrossRef]
27. Mishra, S.; Unnikrishnan, L.; Nayak, S.K.; Mohanty, S. Advances in Piezoelectric Polymer Composites for Energy Harvesting Applications: A Systematic Review. *Macromol. Mater. Eng.* **2018**, *304*, 1800463. [CrossRef]
28. Demartin Maeder, M.; Damjanovic, D.; Setter, N. Lead Free Piezoelectric Materials. *J. Electroceram.* **2004**, *13*, 385–392. [CrossRef]
29. Noheda, B.; Cox, D.E.; Shirane, G.; Gonzalo, J.A.; Cross, L.E.; Park, S.-E. A monoclinic ferroelectric phase in the solid solution. *Appl. Phys. Lett.* **1999**, *74*, 2059–2061. [CrossRef]
30. Vanderbilt, D.; Cohen, M.H. Monoclinic and triclinic phases in higher-order devonshire theory. *Phys. Rev. B* **2001**, *63*, 094108. [CrossRef]
31. Singh, A.K.; Pandey, D.; Zaharko, O. Powder neutron diffraction study of phase transitions in and a phase diagram of (1-x)[$Pb(Mg_{1/3}Nb_{2/3})O_3$]-x$PbTiO_3$. *Phys. Rev. B* **2006**, *74*, 024101. [CrossRef]
32. Cordero, F. Elastic Properties and Enhanced Piezoelectric Response at Morphotropic Phase Boundaries. *Materials* **2015**, *8*, 8195–8245. [CrossRef]
33. Abdullah, A.; Shahini, M.; Pak, A. An approach to design a high power piezoelectric ultrasonic transducer. *J. Electroceram.* **2009**, *22*, 369–382. [CrossRef]
34. Kumar, P.; Thakur, O.P.; Prakash, C.; Goel, T.C. Ferroelectric properties of bulk and thin films of PMNT system. *Phys. B Condens. Matter* **2005**, *357*, 241–247. [CrossRef]
35. Guo, Y.; Luo, H.; Ling, D.; Xu, H.; He, T.; Yin, Z. The phase transition sequence and the location of the morphotropic phase boundary region in $(1-x)$[Pb $(Mg_{1/3}$ $Nb_{2/3})O_3$]–x$PbTiO_3$ single crystal. *J. Phys. Condens. Matter* **2003**, *15*, 77–82. [CrossRef]
36. Choi, S.W.; Shrout, T.R.; Jang, S.J.; Bhalla, A.S. Morphotropic phase boundary in $Pb(Mg_{13}Nb_{23})O_3$-$PbTiO_3$ system. *Mater. Lett.* **1989**, *8*, 253–255. [CrossRef]
37. Levin, A.A.; Pommrich, A.I.; Weissbach, T.; Meyer, D.C.; Zeneli, O.B.J. Reversible tuning of lattice strain in epitaxial $SrTiO_3/La_{0.7}Sr_{0.3}MnO_3$ thin films by converse piezoelectric effect of 0.72$Pb(Mg_{1/3}Nb_{2/3})O_3$-0.28 $PbTiO_3$ substrate. *Appl. Phys.* **2008**, *103*, 054102. [CrossRef]
38. Zhang, S.; Li, F. High Performance Ferroelectric Relaxor-$PbTiO_3$ Single Crystals: Status and Perspective. *J. Appl. Phys.* **2012**, *111*, 031301. [CrossRef]
39. Moorthy, B.; Baek, C.; Wang, J.E.; Jeong, C.K.; Moon, S.; Park, K.; Kim, D.K. Piezoelectric energy harvesting from a PMN–PT single nanowire. *RSC Adv.* **2017**, *7*, 260–265. [CrossRef]

40. Ali, A.; Ali, S.; Shaukat, H.; Khalid, E.; Behram, L.; Rani, H.; Altabey, W.A.; Kouritem, S.A.; Noori, M. Advancements in piezoelectric wind energy harvesting: A review. *R. Eng.* **2024**, *21*, 101777. [CrossRef]
41. Pobering, S.; Ebermeyer, S.; Schwesinger, N. Generation of electrical energy using short piezoelectric cantilevers in flowing media. In *Smart Structures and Materials + Nondestructive Evaluation and Health Monitoring*; International Society for Optics and Photonics: San Diego, CA, USA, 2009; Volume 7288, p. 728807.
42. Bryant, M.; Wolff, E.; Garcia, E. Aeroelastic flutter energy harvester design: The sensitivity of the driving instability to system parameters. *Smart Mater. Struct.* **2011**, *20*, 125017. [CrossRef]
43. Weinstein, L.A.; Cacan, M.R.; So, P.M.; Wright, P.K. Vortex shedding induced energy harvesting from piezoelectric materials in heating, ventilation and air conditioning flows. *Smart Mater. Struct.* **2012**, *21*, 045003. [CrossRef]
44. Pan, C.; Zhang, J.; Xia, H.; Yu, L. A piezoelectric wind energy harvesting device with right-angle cantilever beam. In Proceedings of the 2017 Symposium on Piezoelectricity, Acoustic Waves, and Device Applications (SPAWDA), Chengdu, China, 27–30 October 2017; pp. 255–259.
45. Zeibekis, M.; Vertsioti, G.; Stamopoulos, D. On the optimum processing conditions of $Pb(Zr_xTi_{1-x})O_3$: Revealing the mechanisms to increase the piezoelectric coefficients up to 1100 pm V^{-1}. *J. Phys. D Appl. Phys.* **2016**, *49*, 105304. [CrossRef]
46. Stamopoulos, D.; Zhang, S.J. Experimental estimation of dij coefficients of piezoelectric materials by means of optical microscopy. *EPJ Web Conf.* **2014**, *75*, 09006. [CrossRef]
47. Stamopoulos, D.; Zhang, S.J. A method based on optical and atomic force microscopes for instant imaging of non-homogeneous electro-mechanical processes and direct estimation of dij coefficients in piezoelectric materials at the local level. *J. Alloys Compd.* **2014**, *612*, 34–41. [CrossRef]
48. Vertsioti, G.; Zhang, S.J.; Stamopoulos, D. Pronounced and reversible modulation of the piezoelectric coefficients by a low magnetic field in a magnetoelectric PZT-5%Fe_3O_4 system. *Sci. Rep.* **2019**, *9*, 2178. [CrossRef] [PubMed]
49. Challa, V.R.; Prasad, M.G.; Shi, Y.; Fisher, F.T. A vibration energy harvesting device with bidirectional resonance frequency tunability. *Smart Mater. Struct.* **2008**, *17*, 015035. [CrossRef]
50. Chen, X.; Xu, S.; Yao, N.; Shi, Y. 1.6 V nanogenerator for mechanical energy harvesting using PZT nanofibers. *Nano Lett.* **2010**, *10*, 2133. [CrossRef] [PubMed]
51. Chen, X.; Xu, S.; Yao, N.; Xu, W.; Shi, Y. Potential measurement from a single lead ziroconate titanate nanofiber using a nanomanipulator. *Appl. Phys. Lett.* **2009**, *94*, 253113. [CrossRef]
52. Li, R.; Yu, Y.; Zhou, B.; Guo, Q.; Li, M.; Pei, J. Harvesting energy from pavement based on piezoelectric effects: Fabrication and electric properties of piezoelectric vibrator. *J. Renew. Sustain. Energy* **2018**, *10*, 054701. [CrossRef]
53. Khalili, M.; Biten, A.B.; Vishwakarma, G.; Ahmed, S.; Papagiannakis, A.T. Electromechanical characterization of a piezoelectric energy harvester. *Appl. Energy* **2019**, *253*, 113585. [CrossRef]
54. Gao, M.Y.; Wang, P.; Cao, Y.; Chen, R.; Liu, C. A rail-borne piezoelectric transducer for energy harvesting of railway vibration. *J. Vibroeng.* **2016**, *18*, 4647–4663. [CrossRef]
55. Karimi, M.; Karimi, A.H.; Tikani, R.; Ziaei-Rad, S. Experimental and theoretical investigations on piezoelectric-based energy harvesting from bridge vibrations under travelling vehicles. *Int. J. Mech. Sci.* **2016**, *119*, 1–11. [CrossRef]
56. Wang, H.; Jasim, A.; Chen, X. Energy harvesting technologies in roadway and bridge for different applications—A comprehensive review. *Appl. Energy* **2018**, *212*, 1083–1094. [CrossRef]
57. Chen, N.; Jung, H.J.; Jabbar, H.; Sung, T.H.; Wei, T. A piezoelectric impact-induced vibration cantilever energy harvester from speed bump with a low-power power management circuit. *Sens. Actuators A Phys.* **2017**, *254*, 134–144. [CrossRef]
58. Kim, G.W. Piezoelectric energy harvesting from torsional vibration in internal combustion engines. *Int. J. Automot. Technol.* **2015**, *16*, 645–651. [CrossRef]
59. Esmaeeli, R.; Aliniagerdroudbari, H.; Hashemi, S.R.; Nazari, A.; Alhadri, M.; Zakri, W.; Mohammed, A.H.; Batur, C.; Farhad, S. A rainbow piezoelectric energy harvesting system for intelligent tire monitoring applications. *J. Energy Resour. Technol.* **2019**, *141*, 062007. [CrossRef]
60. Phan, H.; Shin, D.-M.; Jeon, S.H.; Kang, T.Y.; Han, P.; Kim, G.H.; Kim, H.K.; Kim, K.; Hwang, Y.-H.; Hong, S.W. Aerodynamic and aeroelastic flutters driven triboelectric nanogenerators for harvesting broadband airflow energy. *Nano Energy* **2017**, *33*, 476–484. [CrossRef]
61. Wu, N.; Wang, Q.; Xie, X. Wind energy harvesting with a piezoelectric harvester. *Smart Mater. Struct.* **2013**, *22*, 095023. [CrossRef]
62. Orrego, S.; Shoele, K.; Ruas, A.; Doran, K.; Caggiano, B.; Mittal, R.; Kang, S.H. Harvesting ambient wind energy with an inverted piezoelectric flag. *Appl. Energy* **2017**, *194*, 212–222. [CrossRef]
63. Hwang, W.S.; Ahn, J.H.; Jeong, S.Y.; Jung, H.J.; Hong, S.K.; Choi, J.Y.; Cho, J.Y.; Kim, J.H.; Sung, T.H. Design of piezoelectric ocean-wave energy harvester using sway movement. *Sens. Actuators A Phys.* **2017**, *260*, 191–197. [CrossRef]
64. Viet, N.; Xie, X.; Liew, K.; Banthia, N.; Wang, Q. Energy harvesting from ocean waves by a floating energy harvester. *Energy* **2016**, *112*, 1219–1226. [CrossRef]
65. Jung, W.S.; Lee, M.J.; Kang, M.G.; Moon, H.G.; Yoon, S.J.; Baek, S.H.; Kang, C.Y. Powerful curved piezoelectric generator for wearable applications. *Nano Energy* **2015**, *13*, 174–181. [CrossRef]
66. Fan, K.; Liu, Z.; Liu, H.; Wang, L.; Zhu, Y.; Yu, B. Scavenging energy from human walking through a shoe-mounted piezoelectric harvester. *Appl. Phys. Lett.* **2017**, *110*, 143902. [CrossRef]

67. Li, K.; He, Q.; Wang, J.; Zhou, Z.; Li, X. Wearable energy harvesters generating electricity from low-frequency human limb movement. *Micro. Nano Eng.* **2018**, *4*, 24. [CrossRef] [PubMed]
68. Shi, G.; Liang, X.; Xia, Y.; Jia, S.; Hu, X.; Yuan, M.; Xia, H.; Wang, B. A novel dual piezoelectric-electromagnetic energy harvester employing up-conversion technology for the capture of ultra-low-frequency human motion. *Appl. Energy* **2024**, *368*, 123479. [CrossRef]
69. Kim, D.H.; Shin, H.J.; Lee, H.; Jeong, C.K.; Park, H.; Hwang, G.T.; Lee, H.Y.; Joe, D.J.; Han, J.H.; Lee, S.H.; et al. In vivo self-powered wireless transmission using biocompatible flexible energy harvesters. *Adv. Funct. Mater.* **2017**, *27*, 1700341. [CrossRef]
70. Dagdeviren, C.; Yang, B.D.; Su, Y.W.; Tran, P.L.; Joe, P.; Anderson, E.; Xia, J.; Doraiswamy, V.; Dehdashti, B.; Feng, X.; et al. Conformal piezoelectric energy harvesting and storagefrom motions of the heart, lung, and diaphragm. *Proc. Natl. Acad. Sci. USA* **2014**, *111*, 1927. [CrossRef] [PubMed]
71. Hwang, G.T.; Park, H.; Lee, J.H.; Oh, S.; Park, K.I.; Byun, M.; Ahn, G.; Jeong, C.K.; No, K.; Kwon, H.; et al. Self-powered cardiac pacemaker enabled by flexible single crystalline PMN-PT piezoelectric energy harvester. *Adv. Mater.* **2014**, *26*, 4880–4887. [CrossRef]
72. Zhang, Y.; Xu, L.; Liu, Z.; Cui, X.; Xiang, Z.; Bai, J.; Jiang, D.; Xue, J.; Wang, C.; Lin, Y.; et al. Self-powered pulsed direct current stimulation system for enhancing osteogenesis in MC3T3-E1. *Nano Energy* **2021**, *85*, 106009. [CrossRef]
73. Du, S.; Zhou, N.; Gao, Y.; Xie, G.; Du, H.; Jiang, H.; Zhang, L.; Tao, J.; Zhu, J. Bioinspired hybrid patches with self-adhesive hydrogel and piezoelectric nanogenerator for promoting skin wound healing. *Nano Res.* **2020**, *13*, 2525–2533. [CrossRef]
74. Yang, Y.; Xu, L.; Jiang, D.; Chen, B.Z.; Luo, R.; Liu, Z.; Qu, X.; Wang, C.; Shan, Y.; Cui, Y.; et al. Self-powered controllable transdermal drug delivery system. *Adv. Funct. Mater.* **2021**, *31*, 2104092. [CrossRef]
75. Chen, S.; Liu, H.; Ji, J.; Kan, J.; Jiang, Y.; Zhang, Z. An indirect drug delivery device driven by piezoelectric pump. *Smart Mater. Struct.* **2020**, *29*, 075030. [CrossRef]